Radiogenic isotopic and clay mineralogical signatures of terrigenous particles as water-mass tracers: new insights into South Atlantic deep circulation during the Last Termination.

F. Beny[1,2,], V. Bout-Roumazeilles[1], G.R. Davies[2], C. Waelbroeck[3], A. Bory[1], N. Tribovillard[1], M. Delattre[1], R. Abraham[1].*

[1] Laboratoire d'Océanologie et de Géosciences, UMR 8187 CNRS/Univ Lille/ULCO, Cité scientifique, F-59655 Villeneuve d'Ascq, France.

[2] VU University Amsterdam, Department of Earth Sciences, Faculty of Science, De Boelelaan 1085, 1081 HV Amsterdam, The Netherlands.

[3] Laboratoire des Sciences du Climat et de l'Environnement, LSCE/IPSL, UMR 8212 CEA-CNRS-UVSQ, Site de l'Orme des Merisiers, F-91191 Gif sur Yvette Cedex, France

* Corresponding author: beny.francois@gmail.com

Abstract

The past evolution of the Southern Ocean, one of the major components of the climatic system, is still a matter of debate. This study provides new insights into the deep Southern Ocean circulation based on the radiogenic isotopes and clay mineralogical signature of the terrigenous fractions transported by the main deep water masses to sediments recovered in core MD07-3076Q from the central South Atlantic. This approach successfully permits: (1) provenance identification of the various grain-size fractions (clay, cohesive silt and sortable silt); (2) assignment of each grain-size fraction to a specific water-mass; (3) reconstruction of past changes in the main deep water-mass pathways. These data document the evolution of deep-water masses in the South Atlantic Ocean during the last deglaciation. The Antarctic Bottom Water (AABW) speed and northward extension were maximum at the

end of the Last Glacial Maximum (LGM), associated with strong bottom water production in the Weddell Sea, together with a vigorous Lower Circumpolar Deep Water (LCDW). In contrast the North Atlantic Deep Water (NADW) circulation was weaker than today. The onset of the deglaciation (from 17.5 ka to 15 ka, ~Heinrich Stadial 1, HS 1) was marked by weakening and southerly retreat of the AABW and by an increase of mixing between AABW and LCDW. The speed of the AABW remained at its lowest during the Bølling Allerød (B/A) and the Younger Dryas (YD), and the LCDW slowed and retreated to the south, while the NADW progressively migrated southward, deepened, and strengthened between the beginning of the Bølling Allerød and the Holocene (from ~15 to 10 ka).

Keywords

Last Deglaciation; Paleoceanography; Southern Ocean; South Atlantic; Radiogenic isotopes; Clay mineralogy; Grain size distribution.

I. Introduction

The Southern Ocean (SO) is a key area for understanding the present and past carbon cycle. Direct observations indicate that the SO is a sink of atmospheric CO_2 today (Le Quéré et al., 2007; Sallée et al., 2012) while it was likely a source of CO_2 to the atmosphere during the deglaciation (Bouttes et al., 2012; Jaccard et al., 2013). Upwelling of CO_2-rich deep water likely explains most of the CO_2 rise observed during Heinrich Stadials (HS; Ahn and Brook, 2008; Anderson et al., 2009; Fischer et al., 2010; Skinner et al., 2010; Menviel et al., 2014, 2017). Several other processes occurring in the Southern Ocean have also been invoked to explain the deglacial atmospheric CO_2 rise. For example, reduction of biological pump due to reduced iron fertilization (Watson et al., 2000; Wolff et al., 2006; Fischer et al., 2010; Martinez-Garcia et al., 2014); reduced CO_2 solubility due to increased temperature of the ocean (Köhler and Fischer, 2006; Fischer et al., 2010); reduction of sea ice extent (Fischer et

al., 2010). As a consequence, the organization and extension of the Southern Ocean deep water-masses (i.e., Atlantic Meridional Overturning Circulation, AMOC; Skinner et al., 2010; Shakun et al., 2012; Toggweiler et al., 2006) were studied, mainly using paleo-hydrological proxies ($\delta^{18}O$, $\delta^{13}C$, ε_{Nd} of sea water, $\Delta^{13}C$; Barker et al., 2009; Vasquez-Riveiros et al., 2010; Skinner et al., 2010, 2013, 2014; Waelbroeck et al., 2011; Gottschalk et al., 2015b). By contrast, the terrigenous particle signal transported by these deep water-masses in the sub-Antarctic Atlantic Ocean remain poorly studied, even though locally it was successfully used to reconstruct the deep ocean circulation dynamical component (Diekmann et al., 2000 – Scotia Sea; Walter et al., 2000 – Scotia Sea and southwest South Atlantic; Kuhn and Diekmann, 2002 – Cape Basin). In this study, we aim to reconstruct the past evolution of deep-water masses (i.e. contribution to sedimentation, vertical and horizontal extensions, and speeds) during the last deglaciation using the signal carried in the terrigenous particles transported by these water masses. Sediment grain size distribution allows identifying the contribution of distinct oceanic currents (Weltje and Prins, 2007; Weltje, 2012), and reconstructing the speeds of the main deep water-masses (McCave and Hall, 2006; McCave and Andrew, 2019). Grain-size distribution displays distinct modes (Weltje, 2012) that can be attributed to specific physical transport processes (e.g., wind, water currents, ice) and/or transport energy. Because grain-size distribution reflects both carrying vectors (e.g., wind, water currents, ice) and flow speed, several studies focused on the respective isotopic composition of distinct grain-size fractions in order to track distinct provenance patterns (Meyer et al., 2011; Bayon et al., 2015; Beny et al., 2018). Similarly, clay minerals are useful tracers of provenance, erosion balance, weathering, and transportation pattern of fine-grained sediments (Moriarty et al., 1977; Petschick et al., 1996; Kuhn and Diekmann, 2002; Montero-Serrano et al., 2010). Finally, radiogenic isotope compositions of sediments can be used to

73 decipher the different provenances of terrigenous particles and determine their respective
74 contributions through time (Walter et al., 2000; Bayon et al., 2009).

75 This study focuses on the South Atlantic Ocean, where northern water-masses (North
76 Atlantic Deep Water, NADW) and southern ones (Lower Circumpolar Deep Water, LCDW
77 and Antarctic Bottom Water, AABW) mix, because this area is key for understanding the
78 atmosphere-ocean exchanges that control CO_2 sequestration/outgassing. The reorganization of
79 these deep water-masses during the deglaciation is still a subject of debate and their impact on
80 deglaciation is not resolved (Barker et al., 2009; Skinner et al., 2010, 2013; Waelbroeck et al.,
81 2011; Adkins, 2013; Menviel et al., 2014, 2015a,b, 2018). Recent studies of the last
82 deglaciation ventilation events in the South Atlantic Ocean demonstrated an apparent synergy
83 between physical and biological processes (Gottschalk et al., 2016), whereas chemical and
84 physical processes appear to be decoupled (Roberts et al., 2016). These contrasting results
85 highlight the lack of constraints on the dynamical aspect of the water-masses mixing. In this
86 paper, we combined grain-size distribution, clay mineralogy, and radiogenic isotope (Sr-Nd-
87 Pb) analyses (on separated grain-size fractions) in order to investigate the evolution
88 (horizontal and vertical extensions, pathways, speed) of deep-water-masses in the South
89 Atlantic Ocean during the last termination.

II. General setting

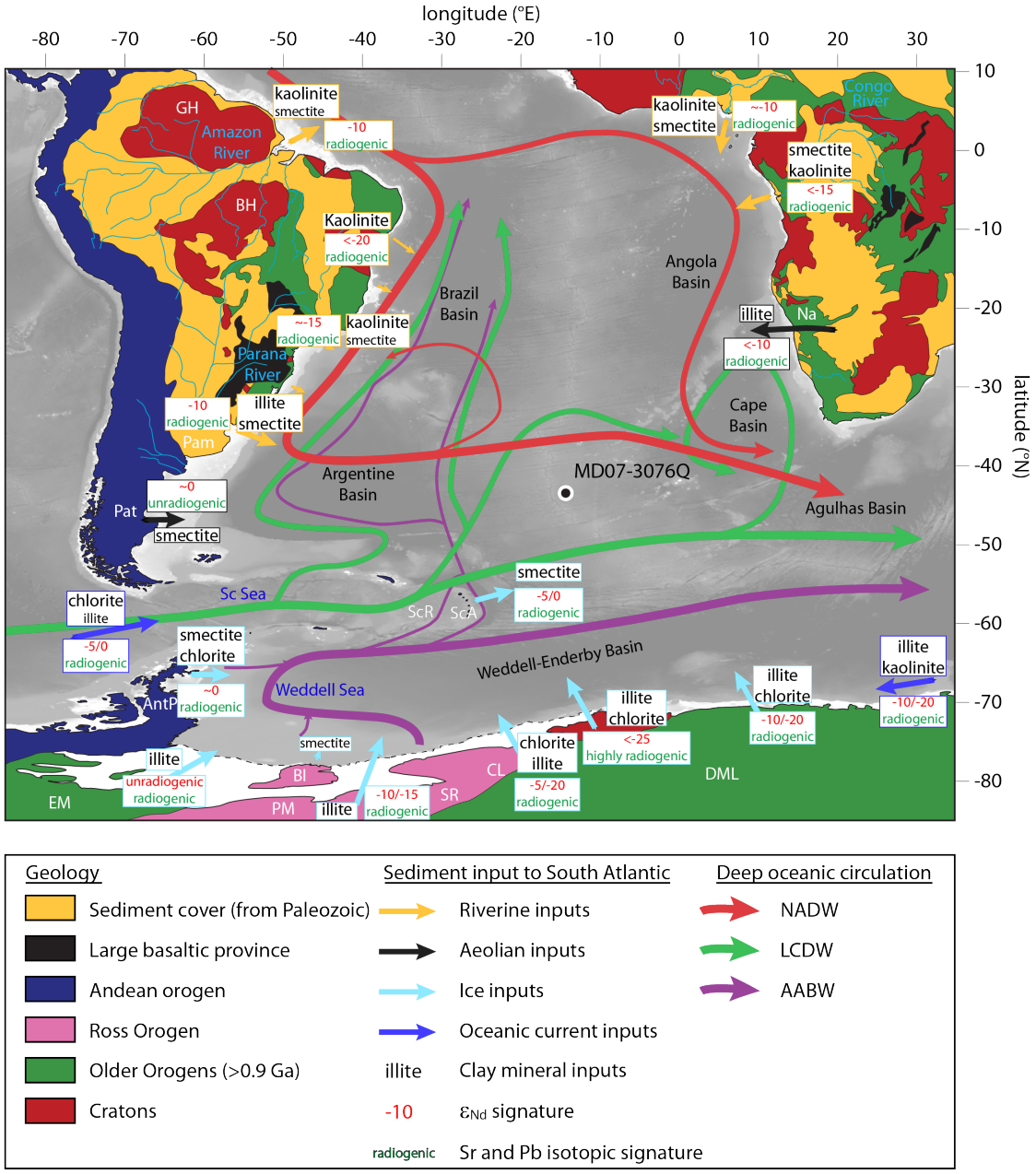

Figure 1: Simplified geological map of the study area. Light blue text names riverine systems, dark blue text names seas, black text names oceanic basins, and white abbreviations names areas. In South America: Guyana Highlands -GH-, Brazilian Highlands -BH-, Argentinian Pampas -Pam-, Patagonia -Pat-; in Africa: Namibian deserts-Na-; in Antarctica: Ellsworth Mountains -EM-, Antarctic Peninsula -AntP-, Pensacola Mountains -PM-, Berkner Islands -BI-, Shackleton Range -SR-, Coats Land -CL-, Dronning Maud Land -DML-. Clay

mineral inputs to the South Atlantic Ocean derived from the studies of Petschick et al. (1996);Diekmann et al. (2000); Walter et al. (2000); Guyot et al. (2007); Bayon et al. (2016); and Khondoker et al. (2018).

A. Deep water-masses

Modern South Atlantic deep circulation is characterized by the incursion of the NADW into the Southern Ocean, where it mixes/interacts with both the AABW and the Circumpolar Deep Water (CDW; figure 1). The southward NADW mainly flows as Deep Western Boundary Current along the South American Margin before leaving the continental shelf and flowing eastward around 45°S (Reid, 1989; Larqué et al., 1997; Stramma and England, 1999). A branch of the NADW crosses the Atlantic Ocean at the equator before to flow southward along the African margin and to reach the Indian Ocean via the Good Hope Cape (Larqué et al., 1997). In the Southern Ocean, NADW flows between two parts of the CDW: the Upper Circumpolar Deep Water (UCDW) flows above, whereas the Lower Circumpolar Deep Water flows underneath. The northern extension of the UCDW is very asymmetric with larger extent in the eastern part of the South Atlantic (Larqué et al., 1997). On the west side of the Mid-Atlantic Ridge (MAR), the LCDW penetrates into the Argentine Basin via the Drake Passage and flows northward into the Brazil Basin (Speer and Zend, 1993). On the east of the MAR, the LCDW is a major oceanic feature in the Cape Basin, where it becomes diluted in the Angola Basin (Larqué et al., 1997). The lower part of the LCDW is currently mixed with the upper part of the AABW (Orsi et al., 1999) that is produced heterogeneously along the Antarctic Shelf (Foster and Carmack, 1975; Orsi et al., 1999). Foster and Camarck (1975) demonstrated the formation of a very cold type of bottom water in the vicinity of the shelf break (the Polynyas mode) between 29 and 40°W and along the Antarctic Peninsula's tip, between 35 and 55°W and north of 65°S. Today this production occurs mainly in winter when seawater is close to freezing and becomes saltier due to sea ice

formation (Foster and Camarck, 1975; Orsi et al., 1999), which increases its density and promotes convection. This mode is called the Polynyas mode. However, in the Weddell Sea, a second mode of bottom water formation occurs: the Ice Shelf Water mode, which corresponds to bottom water formation under the Antarctic ice shelves due to super-cooling (Krueger et al. and references therein, 2012). The AABW is very thick in the Weddell-Enderby Basin (more than 4000 m; Orsi et al., 1999) and is partially exported to the Argentine Basin via the eastern Scotia Sea (east and west of the South Sandwich Islands) toward the Brazil Basin via the Vema Channel, and to the Agulhas and Crozet basins (Stramma and England, 1999). The AABW is a dominant oceanic feature south of 50°S although its' northern influence extents to around 10°S (Reid et al., 1989).

The characteristics of deep water masses were not constant through time and the evolution of the AMOC is controversial (Weber and Drijfhout, 2007; Vasquez Riveiros et al., 2010; Waelbroeck et al., 2011; Howe et al., 2016). Some studies have suggested that during the Last Glacial Maximum (LGM) the NADW was as strong as today but shallower (Curry and Oppo, 2005; Gherardi et al., 2009). Other studies suggest that it was weaker and shallower (Menviel et al., 2012; Howe et al., 2016). The NADW southern extension seems limited during glacial times, whereas southern-born water-masses extended further north (Kuhn and Diekmann, 2002; Skinner et al., 2013). Similarly, modifications of the Antarctic Circumpolar Current (ACC, including the CDW) during the last climatic cycle are still debated. Some studies reported severe modifications of the ACC intensity in the Atlantic (Noble et al., 2012) and Indian (Dezileau et al., 2000; Mazaud et al., 2010) sectors of the Southern Ocean: the activity of the ACC increased during the LGM, probably linked to enhanced westerly winds (Dezileau et al., 2000; Walter et al., 2000; Mazaud et al., 2010). In contrast, other studies support insignificant modification of the ACC in the Atlantic sector of the Southern Ocean (Gersonde et al., 2003) and Drake Passage (McCave et al., 2014). Finally,

148 the evolution of the AABW is also uncertain. Krueger et al. (2012) suggests that the
149 production of AABW was similar during glacial and interglacial, but dropped during
150 terminations (including the last deglaciation). In addition, Menviel et al. (2017) suggest that
151 the "AABW" (corresponding to CDW and AABW in our study) was weaker during the LGM
152 than today. In contrast, other studies suggest enhanced northward flow of AABW via deep
153 western boundary currents in all three major ocean (Pacific: Hall et al., 2001; Govin et al.,
154 2009; Indian: Govin et al., 2009; Atlantic: Govin et al., 2009; Spooner et al., 2018).

155 Any modifications of the AMOC have a potential effect on carbon storage/outgassing
156 that is tightly controlled by ocean stratification/ventilation, itself resulting from contrasting
157 physical and chemical properties of the water-masses. High ocean stratification – as during
158 the last glacial – inhibits vertical mixing and isolates the deep ocean from the atmosphere. In
159 contrast, ventilation events – breakdown of the stratification that occurred during the last
160 deglaciation – allow CO_2 to upwell from the deep ocean and to be rapidly transferred to the
161 atmosphere (Toggweiler et al., 2006; Barker et al., 2010; Skinner et al., 2010, 2013, 2014;
162 Burke and Robinson, 2012).

163 B. Geological setting

164 The Atlantic sector of the Southern Ocean may receive sediments from Antarctica, the
165 Scotia Sea area (i.e., Scotia Arc, southern Patagonia, and northern Antarctic Peninsula) South
166 America, and Africa. Here, we present the general geological structure of these areas, and
167 their respective isotopic signatures (figure 1).

168 Antarctica corresponds to two distinct geological domains: East and West Antarctica.
169 West Antarctica includes the Ellsworth Mountains (EM), the Antarctic Peninsula (Ant P), the
170 Scotia Arc region (SCA). The geology of the Ellsworth Mountains (figure 1) is poorly known
171 due to the lack of outcrop. These mountains are composed of Precambrian rocks,
172 corresponding mainly to granodiorite orthogneiss intruded by granitic and pegmatitic sheets

(Tingey et al., 1991). The isotopic composition of the area is not known, but the age of the rock suggests radiogenic Sr and Pb isotope ratios, and unradiogenic ε_{Nd} (figure 1). This area mostly delivers illite to the sea (Petschick et al., 1996; figure 1). The Antarctic Peninsula, composed of alkaline and calcalkaline magmatic rocks associated with deformed sediments of similar composition (Anderson, 1965; Tingey et al., 1991), is a potential source of terrigenous sediment for CDW and AABW. The Antarctic Peninsula is characterized by radiogenic ε_{Nd}, and low Sr and high Pb isotope ratios (figure 1). Clay minerals from this area mostly correspond to well-crystallized smectite (crystallinity around 1.5, Petschick et al., 1996; figure 1), and chlorite. The Scotia Arc islands rocks are similar to those of the Antarctic Peninsula but with slightly more radiogenic Nd, and slightly less radiogenic Sr and Pb (figure 1). This area exports exclusively well-crystallized smectite to the ocean (crystallinity lower than one; Petschick et al., 1996).

The East Antarctic domain is an old shield with rocks > 0.9 Ga. Rocks from the Pensacola Mountains (PM) to the Shackleton Range (SR) represent the Ross Orogen (i.e., Transantarctic Mountains) and are mainly composed of varied metamorphic rocks aged from the Late Proterozoic to Late Paleozoic (Barrett, 1991; Laird, 1991; Tingey, 1991; Hauptvogel and Passchier and references therein, 2012). The isotopic composition of the area is characterized by unradiogenic Nd, with intermediate to high Sr isotope ratios (figure 1). The Pb isotope composition unknown, as is the case for most of East Antarctica rocks. The few studies reporting Pb isotope ratios have been carried out on feldspars only. The area releases mostly illite and chlorite (Petschick et al., 1996). Smectite is also exported from the Berkner Island, but is found only locally (Petschik et al., 1996). To the east, the Grenville Belts (920 to 1330 Ma) outcrop on the Coats Land (CL) and western Dronning Maud Land (WDML) with a wide range of gneissic and clastic sediments (Capurro, 1955; Anderson, 1965; Tingey et al., 1991) with unradiogenic Nd, and radiogenic Sr isotope ratios (figure 1). Clay minerals

198 produced in this area are mainly chlorite and illite (Petschick et al., 1996). In the northernmost
199 part of the Dronning Maud Land, the old Grunehogna Craton is composed mainly of Archean
200 granitoids (Tingey et al., 1991; Mieth and Jokat, 2014; Pierce et al., 2014) with very
201 unradiogenic Nd (ε_{Nd}<< -20) and radiogenic Sr ratios (figure 1). The clay minerals generated
202 in that area are mainly chlorite and illite (Petschick et al., 1996).

203 South America can be divided into two blocks: the recent Andean Orogen, and the old
204 South American Shield. In the Atlantic Sector of the Southern Ocean, the Andean Orogen
205 mostly corresponds to Patagonia (Pat). The geology and the isotopic composition of this
206 region is similar with the Antarctic Peninsula: radiogenic Nd, unradiogenic Sr and Pb isotope
207 ratios, but with higher $^{207}Pb/^{204}Pb$ than the Antarctic Peninsula (figure 1; Olivero and
208 Martinioni, 2001; Sayago et al., 2001 and references therein; Smith et al., 2003; Khondoker et
209 al., 2018). Even if the climate is slightly more humid than in the Antarctic Peninsula,
210 Patagonia also produces mainly well-crystallized smectite (Petschick et al., 1996; Desiage et
211 al., 2018; Khondoker et al., 2018).

212 The South American Shield is composed of several cratonic areas separated by vast
213 ancient orogenic belts. (Cordani and Sato, 1999; Engler, 2009; Oyhantçabal and Siegesmund,
214 2011; Siegesmund et al., 2011; de Alkmim, 2015). Cratonic areas are mainly composed of
215 granitoids and a wide range of metamorphic rocks, while orogenic belts are composed of a
216 large variety of metamorphic rocks with high original composition (from the granite to the
217 ophiolite and the juvenile magmatic arc; Almeida et al., 1981; Barros et al., 1982; Moura and
218 Gaudette, 1993; Neves, 2003; de Alkmim, 2015; Nogueira et al., 2007; Pimentel et al., 2011;
219 Fuck et al., 2014; McGee et al., 2015; D'el-Rey Silva et al., 2016). The overall isotopic
220 composition of the South American Shield is radiogenic Sr and Pb, and very unradiogenic Nd
221 isotope ratios (figure 1). South of the South American Shield, a large tholeiitic-basaltic
222 province is known as the Parana basalt (Waichel et al., 2012; Milani and Ramos, 2017). The

composition of the Parana basalts differs from the South American Shield with radiogenic Nd, and very low $^{87}Sr/^{86}Sr$ ratio (<0.5; Tapani Ramo et al., 2016).

This South American Shield is drained by important riverine systems such as the Amazon and Parana rivers. The Amazon drains sediments from the Andes, as well as the South American Shield. The South American Shield is characterized by rocks with unradiogenic Nd and radiogenic Sr and Pb (figure 1). The clay mineral exported to the ocean is mainly kaolinite (Petschick et al., 1996; Guyot et al., 2007; Bayon et al., 2015). However, sediments are mainly exported northwards toward the Caribbean Sea. The Parana River drains the southern part of the South American Shield, the Parana basalts, and the north of Patagonia. Its isotopic composition has intermediate Nd, Sr, and Pb isotope ratios (figure 1). Clay minerals transported via this river are illite (~60%; Petschick et al., 1996; Campodonico et al., 2016), kaolinite, and smectite. Other smaller rivers drain the south of Brazil, and mainly deliver sediments characterized by unradiogenic Nd, and radiogenic Sr and Pb isotope ratios, containing mainly smectite derived from the Parana basalts and kaolinite (figure 1; Petschick et al., 1996). On the other hand, Patagonia and Pampas are dry and windy areas (Clapperton, 1993). Consequently, part of the detrital particles is exported to the ocean via aeolian processes as loess (Mathias et al., 2014). The overall isotopic composition of this smectite-rich loess is radiogenic Nd, unradiogenic Pb and Sr ratios. According to Mathias et al. (2014), the sediment delivery to the southwest Atlantic is currently dominated by loess, and by the Parana River sediments.

A large proportion of the African continent comprises Archean Cratons (western Africa, Congo), and rocks related to the Pan African Orogen. The cratons are composed of gneisses while the Pan African Orogen is mainly composed of flysch deposits associated with volcanic formations, and intruded by granitoids. The overall geochemical composition of Africa is intermediate to very unradiogenic Nd, and intermediate to very radiogenic Sr and Pb

isotope ratios (figure 1). Clay minerals formed in the Congo depression are mainly poorly crystallized smectite and kaolinite, whereas the Namibian deserts release illite-rich loess (Bremner and Willis, 1993; Petschick et al., 1996; Bayon et al., 2015; figure 1).

III. Material and methods

A. Material

This study is based on sediment samples from core MD07-3076Q (44°9.2'S, 14°13.7'W) recovered by the French Vessel *Marion Dufresne* in 2007 on the eastern flank of the Mid-Atlantic Ridge at 3770 m depth (figure 1). The core chronology is based on planktonic foraminifer radiocarbon dates (30 measurements for the studied interval) and stratigraphic control points (Skinner et al., 2010, 2013, 2014; Gottschalk et al, 2015b). Today, the site is bathed in the LCDW. From the seafloor to the surface, the water masses observed in the water column above the study site are the LCDW, NADW, UCDW, and intermediate and surface waters. In nearby deeper oceanic basins, the AABW is also found, and it is thought that particles transported by this bottom water can reach our site by advection and mixing with the LCDW.

B. Sample preparation and analytical procedure

All samples were first decarbonated using 0.1N HCl and then deflocculated by repeated washing using pure water.

1. Grain-size distribution

Grain-size distribution was measured on carbonate-free sediment using a Malvern Mastersizer 2000 laser (0.02-2000 μm) following standard protocols (Montero-Serrano et al., 2009). The clay-size fraction corresponds to the proportion (in volume) of particles with a diameter smaller than 2 μm, the cohesive silts correspond to the 2 to 10 μm diameter

particles, the sortable silts correspond to the 10 to 63 μm diameter particles, and the sand fraction to the particles coarser than 63 μm.

2. Clay mineralogy

The clay-size fraction (< 2μm) was isolated by differential settling according to Stoke's Law. This fraction was then concentrated by centrifugation (40 minutes, 3500 rotation per minute) and an aliquot was placed on glass slides. X-ray diagrams were obtained using a Bruker D4Endeavor (standard 30 kV and 30 mA). Each sample is run three times between 2.49 and 32.5°2θ: (1) dried sample, (2) glycolated sample (12 hours in ethylene glycol), and (3) heated sample (490°C for 2 hours). The proportion of each clay mineral (smectite, chlorite, illite, and kaolinite) is determined using the main X-ray diffraction peaks (layer and interlayer) on X-ray spectra according to their crystallographic characteristics (Brown, 1980). Smectite is characterized by a main peak at 14-15 Å on the air-dried samples that expands at 17 Å after ethylene glycol saturation and collapses at 10 Å after heating. Illite is characterized by a main peak at 10 Å on the three runs. Kaolinite and chlorite are measured based on their main peak at 7-7.2 Å and further distinguished using pseudo-void deconvolution of the kaolinite/chlorite doublet at 3.54/3.58 Å. All measurements and semi-quantitative estimations are processed using the McDiff software (Petschick, 2000). The index of Esquevin (Esquevin, 1969) corresponds to the ratio between the intensity of the peak of illite at 5 Å and at 10 Å (illite 5Å/10Å). In this study, the crystallinity of illite and smectite has been measured using the method of integral breath to enable comparison with the work of Petschik et al. (1996) in the South Atlantic. High crystallinity (high values of the index) corresponds to badly crystallized mineral.

3. Isotope Analysis

The grain-size distribution recognized three distribution modes. These three grain-size fractions were then isolated in order to examine their provenance. The clay-size fraction (0-

296 2 μm) was isolated by repeated extractions by settling. The coarse fraction (20-40 μm in the
297 old section of the core before 11.5 ka cal BP, noted hereafter as ka, and 20-32 μm after 11.5
298 ka) was isolated by sieving the clay-free residue. The 2-20 μm grain-size fraction is thus the
299 residue of clay separation and coarse fraction sieving. An aliquot of 10 to 150 mg (depending
300 of the sediment quantities available) was then used for chemical procedures.

301 Chemical and isotopic measurements were performed at the Faculty of Science of the
302 Vrije Universiteit, Amsterdam. Sediment was digested in closed Savillex^{TM} Teflon beakers
303 using a mixture of concentrated HF and HNO_3 (~2/3 and 1/3, respectively) for a few days at
304 120°C. After digestion, samples were dried out and re-dissolved in ~6.5N HCl to remove
305 fluorides. Nd, Sr, and Pb were purified using conventional ion chromatography. Pb isotopes
306 were processed first and purified using AG-X8 200-400 mesh resin. Light rare earth elements
307 (LREE) were isolated using true-spec resin medium (Eichrom^{TM}, 100-150 μm mesh size) and
308 Nd was eluted from the LREE fraction using LN-resin (Eichrom^{TM}, 50-100 μm mesh size). Sr
309 was recovered using Sr resin column. Nd and Pb measurements were performed by bracketing
310 using respectively CIGO and NBS981 standards on Thermo Scientific Neptune multi-
311 collector inductive coupled plasma-mass spectrometer (MC-ICPMS), whereas Sr
312 measurements were performed on a thermal ionization multi-collector-MS (TIMS). Due to
313 relatively low content of Nd in some of the coarse grain-size fraction (20-32/40μm), Nd
314 measurements of these fractions were also performed by TIMS.

IV. Results

A. Grain-size distribution

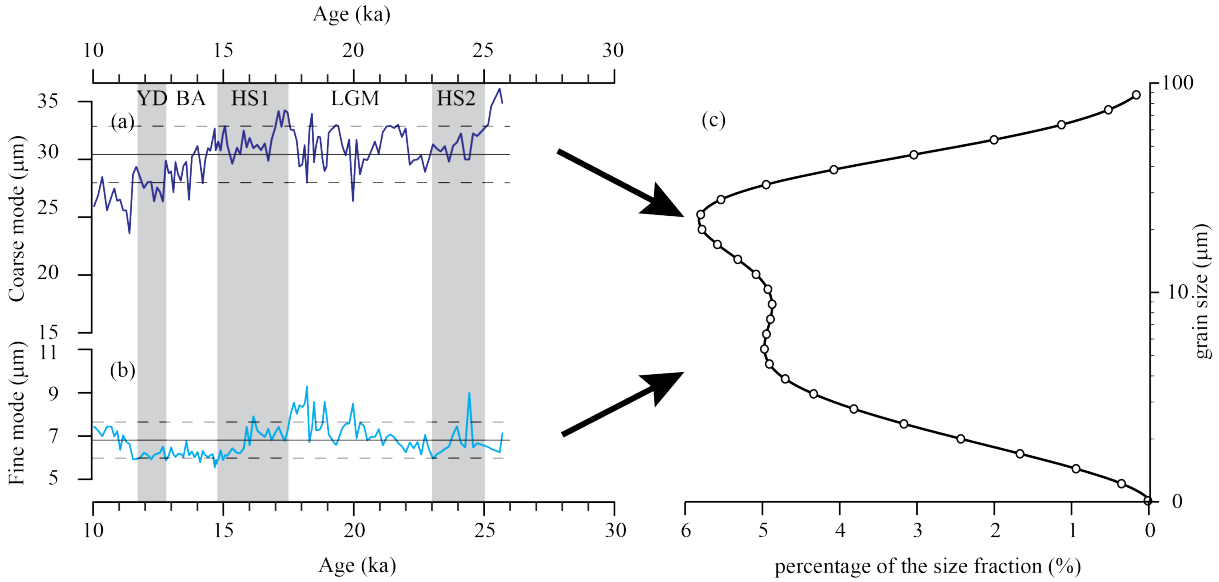

Figure 2: Grain-size results from core MD07-3076Q. (a) and (b) Variation of the coarse and fine grain size mode values, respectively, through time. Black lines represent the average value for both grain-size modes while dashed lines represent their standard deviation; (b) typical grain-size distribution curve from the core MD07-3076Q. Two grain-size modes can be identified from the grain-size distribution curve. YD: Younger Dryas, BA: Bølling Allerød, HS: Heinrich Stadial; LGM: Last Glacial Maxima.

The grain-size distribution is bimodal throughout the core (figure 2) with a coarse mode ranging in the sortable silts fraction (from 23.6 and 36.2 μm, average: 30.4, standard deviation: 2.48; table 1) and a fine mode ranging in the cohesive silts fraction (from 5.6 and 9.3 μm, average: 6.8, standard deviation: 0.8; table 1). The sortable silt (10-63 μm) fraction is dominant (41 to 52% in volume of the total terrigenous fraction, average: 47%, standard deviation: 2.4; table 1) and the cohesive silts (2-10 μm) represent 35 to 45% (average: 39%, standard deviation: 2.4; table 1). The clay (<2 μm) and sand fractions (>63 μm) represent

331 respectively 2 to 5% (average: 3.4%, standard deviation: 0.7; table 1) and 1 to 6% (average:
332 3.0, standard deviation: 1.0; table 1) of the total terrigenous fraction (table 1).

333 In details, the mean of the coarse mode (hereafter mentioned as the sortable silt mode)
334 is slightly coarser during the LGM (figure 2.a), and decreases during the deglaciation and
335 reaches its minimum values after the Younger Dryas (YD). The average size of the fine mode
336 (hereafter mentioned as the cohesive silt mode) is maximum at the end of the LGM and
337 displays its lowest values during the deglaciation (figure 2.b).

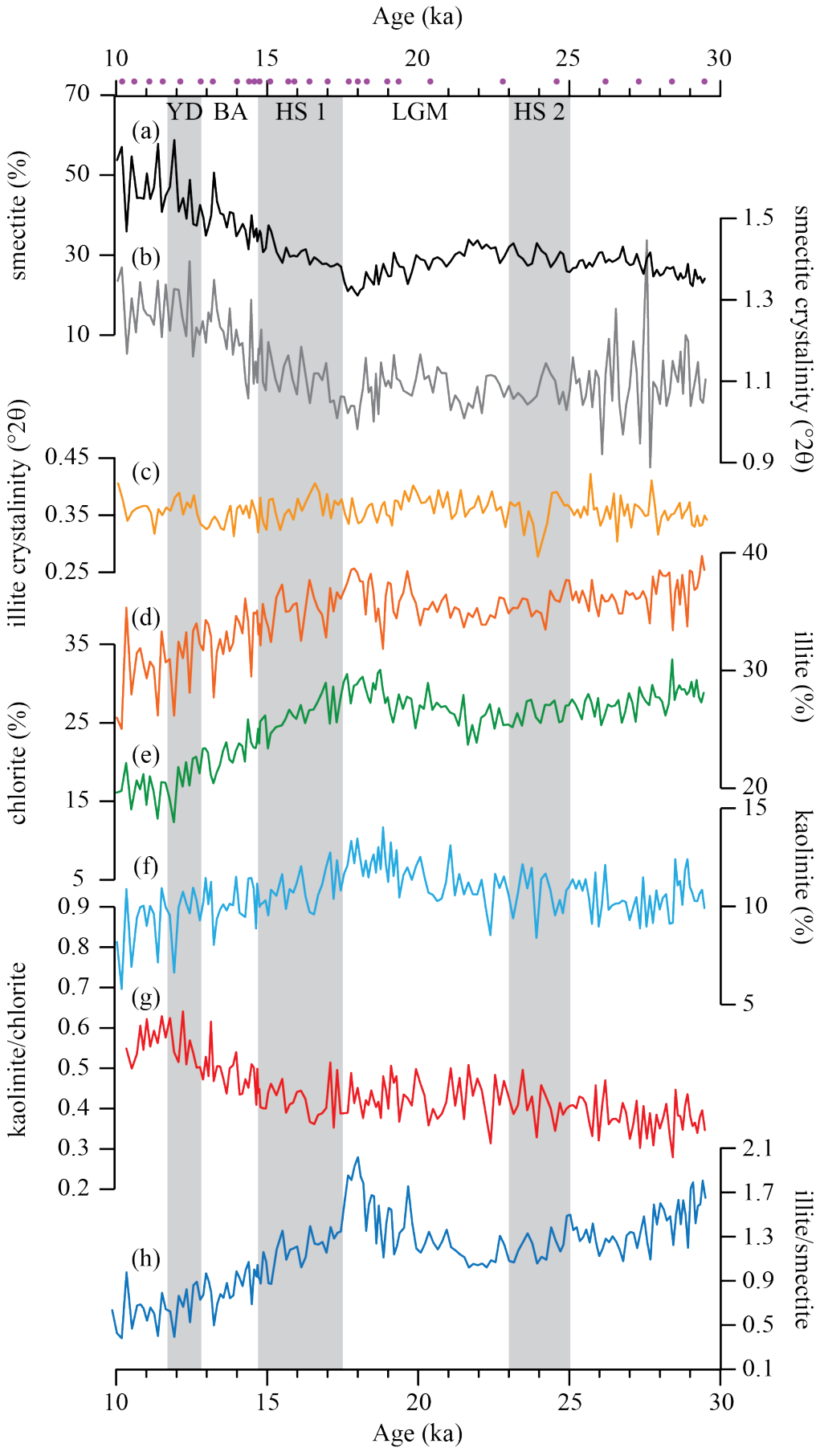
Age (ka)
10
15
20
25
30
YD
BA
HS 1
LGM
HS 2
(a)
(b)
(c)
(d)
(e)
(f)
(g)
(h)
smectite (%)
smectite crystalinity (°2θ)
illite crystalinity (°2θ)
illite (%)
chlorite (%)
kaolinite (%)
kaolinite/chlorite
illite/smectite

338

Figure 3: Clay mineral data from core MD07-3076Q. Purple dots represent the radiocarbon dates used for the age model. (a) relative proportion of smectite (%); (b) smectite crystallinity (°2θ); (c) illite crystallinity (°2θ); (b) and (c) note that the lower is the crystallinity index, the better the mineral is crystallized; (d) relative proportion of illite (%); (e) relative proportion of chlorite (%); (f) relative proportion of kaolinite; (g) kaolinite/chlorite ratio (K/C); (h) illite/smectite ratio (I/S).

B. Clay Mineralogy

The clay mineral assemblage is composed of smectite ((S) 18-59%; figure 3.a), illite ((I) 21-40%; figure 3.d), chlorite ((C) 12-33%; figure 3.e), and kaolinite ((K) 5-14%; figure 3.f) with higher smectite content at the end of the deglaciation, and higher illite, chlorite and kaolinite contents during the LGM. The smectite crystallinity ranges from 0.89 and 1.45 (figure 3.b) and varies in phase with the smectite content with slightly higher variability between 25 and 30 ka. The illite crystallinity varies between 0.27 and 0.42 (figure 3.c and 4) without major variation. Clay mineral proportions are relatively stable during the LGM but records a shift during the deglaciation with an increase of smectite compared to the other clay minerals. The smectite crystallinity varies simultaneously with smectite proportion changes. The K/C ratio is stable during the LGM, and increases during the deglaciation. The I/S ratio presents two maxima at the beginning of the record and at the end of the LGM, sharply decreases at the beginning of the HS 1, and steadily decreases during the deglaciation.

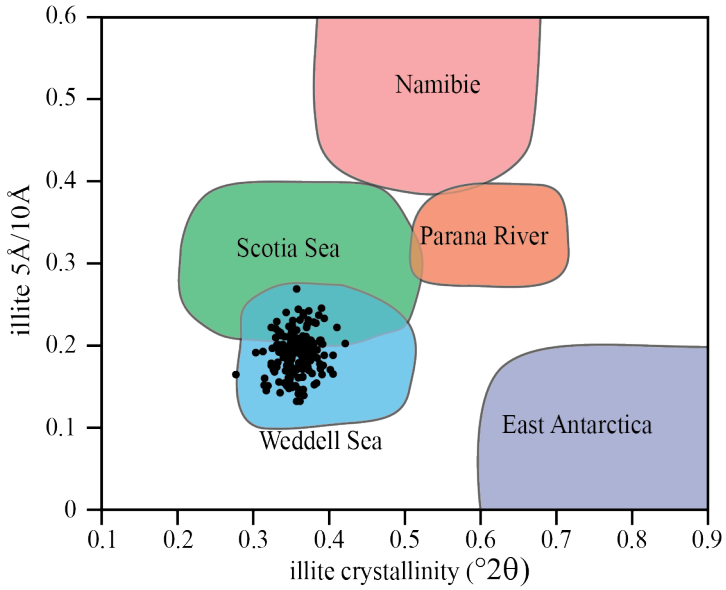

Figure 4: Crystallographic properties of illite from site MD07-3076Q (black dots) and comparison with properties of illite from potential sources to the South Atlantic basin. The data used for comparison are from Petschick et al., (1996). Illite 5Å/10Å ratio gives information on the chemical properties of illite (Fe-Mg- vs Al-rich illite) while the crystallinity gives clues on the quality of the mineral crystal (high crystallinity: badly crystallized mineral).

C. Radiogenic Isotopes

Isotopic results are presented for the sortable silt mode fraction (20-32/40 μm) and the cohesive silt mode fraction (2–20 μm) and for the clay-size fraction (<2 μm) (tables 2 to 4). Lead isotope ratios were only been measured on the clay-size fraction (table 2).

1. Clay-size fraction (<2 μm)

The ε_{Nd} of the clay-size fraction ranges from -7.2 to -4.8. It is relatively stable during the last glacial (<± 0.5 ε_{Nd}), decreases by 2 ε units during the deglaciation and shows minimum values at the end of the deglaciation (figure 5.c). The $^{87}Sr/^{86}Sr$ ratio ranges from 0.711 to 0.712: it is rather high and stable (<± 0.0003), during the last glaciation and displays a rapid decrease at ~15 ka. The ratio records a short rebound at 12.7 ka before reaching its

minimum values at the end of the deglaciation (0.7107; figure 5.d). The $^{87}Sr/^{86}Sr$ ratio and the ε_{Nd} show a similar temporal evolution (they both decrease during the deglaciation), which is surprising as in nature they usually record opposite relationship. The three Pb isotope ratios record their lowest values around 25 ka, and increase thereafter. This trend is more pronounced for the $^{207}Pb/^{204}Pb$ ratio during the deglaciation. Some fluctuations of the three ratios are observed during the deglaciation with higher ratios at climatic transitions (LGM/Heinrich Stadial 1 –HS1–, HS1/Bølling-Allerød – B-A – , B-A/Younger Dryas –YD–, Holocene onset), and low values during the middle of the HS1, the middle of the B-A, and the second half of the YD (except for the $^{206}Pb/^{204}Pb$). We note that the Sr isotope rebound observed at 12.7 ka is also associated with variations Pb isotope ratios.

2. Cohesive silt mode fraction (2-20 μm)

The ε_{Nd} of the 2-20 μm grain-size fraction (cohesive silt mode fraction) ranges from -5.5 to -3.9 with the lowest values at 13, 18, 23 and 29 ka (figure 5.b). The $^{87}Sr/^{86}Sr$ ratios are generally constant with higher values around 13, 19, and 24 ka (figure 5.f).

3. Sortable silt mode fraction: (20-32/40 μm)

The ε_{Nd} of the sortable silt mode fraction ranges from -4.9 to -1.4. Values are relatively unchanging during the last glacial period (-2 ± 0.5 ε_{Nd}) but decreases after 18 ka and reaches a minimum (-5) at the end of the deglaciation (figure 5.a). The $^{87}Sr/^{86}Sr$ ratio ranges from 0.708 and 0.710. $^{87}Sr/^{86}Sr$ values are lower during the HS 2, at the beginning of the HS 1, and at the beginning of the YD, while the highest value is recorded at the B-A offset (figure 5.e).

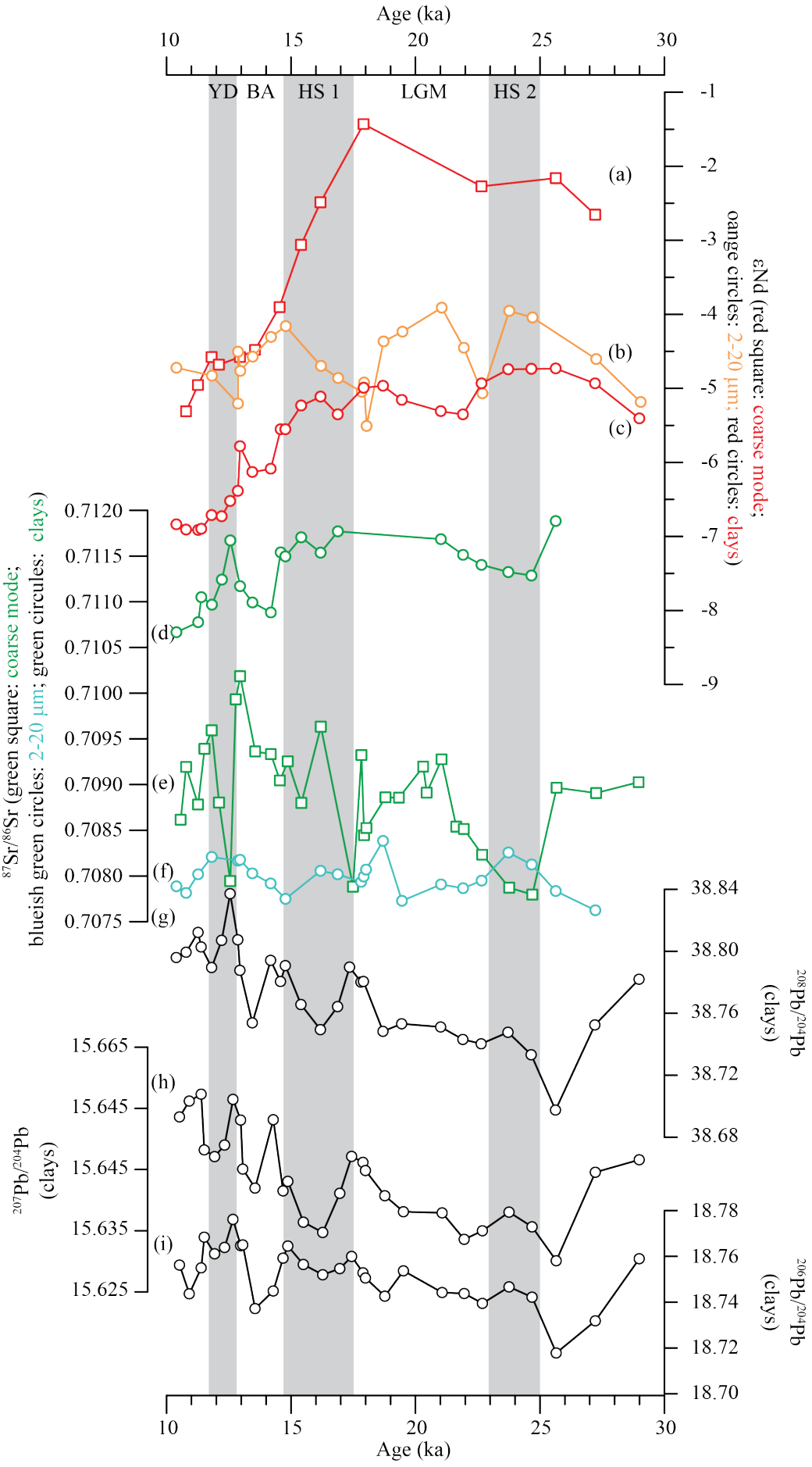
Age (ka)
10
15
20
25
30
YD
BA
HS 1
LGM
HS 2
(a)
(b)
(c)
(d)
(e)
(f)
(g)
(h)
(i)
εNd (red square: coarse mode; oange circles: 2-20 μm; red circles: clays)
-1
-2
-3
-4
-5
-6
-7
-8
-9
87Sr/86Sr (green square: coarse mode; blueish green circles: 2-20 μm; green circules: clays)
0.7120
0.7115
0.7110
0.7105
0.7100
0.7095
0.7090
0.7085
0.7080
0.7075
208Pb/204Pb (clays)
38.84
38.80
38.76
38.72
38.68
207Pb/204Pb (clays)
15.665
15.645
15.645
15.635
15.625
206Pb/204Pb (clays)
18.78
18.76
18.74
18.72
18.70
Age (ka)
10
15
20
25
30

396

Figure 5: Isotopic results from core MD07-3076Q. (a) ε_{Nd} from the sortable silt mode fraction (20-32/40 μm); (b) ε_{Nd} from the cohesive silt mode fraction (2-20 μm); (c) ε_{Nd} from the clay-size fraction (<2 μm); (d) $^{87}Sr/^{86}Sr$ from the clay-size fraction (<2 μm); (f) $^{87}Sr/^{86}Sr$ from the sortable silt mode fraction (20-32/40 μm); (g) $^{87}Sr/^{86}Sr$ from the cohesive silt mode fraction (2-20 μm); (h) $^{208}Pb/^{204}Pb$, (i) $^{207}Pb/^{204}Pb$, and (j) $^{206}Pb/^{204}Pb$ from the clay-size fraction (<2 μm).

V. Discussion

A. Sediment provenance

1. Clay size fraction: an overall provenance signal

To determine the provenance of this grain-size fraction, both clay mineral proportions and radiogenic isotopes have been used. Kaolinite and chlorite have distinct provenances: at present, kaolinite is mainly found at low latitudes where chemical weathering is strong. Brazilian rivers (Amazon and Parana), as well as equatorial and tropical African rivers are characterized by high contents of kaolinite (figure 1). Inherited kaolinite is also found in East Antarctica marine sediments (figure 1), but is transported by the westward Antarctic Coastal Current and remains trapped in the Weddell-Enderby Basin due to the Weddell Gyre circulation (Petschick et al., 1996) and this kaolinite is therefore unlikely to contribute to sedimentation at the studied site. Consequently, kaolinite can be used to trace the low latitude provenance. Conversely, presently, chlorite mainly characterizes high latitude regions, where weak chemical weathering allows its preservation. It is abundant in Antarctica and the Scotia Sea (figure 1). Consequently, chlorite can be considered a tracer of high latitude provenance. Thus, the kaolinite/chlorite ratio (K/C) discriminates southern-born versus northern-born material in the southern Atlantic (Petschick et al., 1996; Kuhn and Diekmann., 2002; Kruger et al., 2008).

421 Illite provenance is more complex. It is very abundant in the Weddell Sea, Namibian
422 deserts, the Parana River (60% of the delivered sediment), and it is also present, although at
423 lower concentrations (<30%), in the Scotia Sea (figure 1). To decipher the provenance of
424 illite, we used the chemical (5/10Å ratio, i.e., Fe-Mg vs. Al rich illite) and crystallographic
425 properties (crystallinity) of this mineral. Data are compared with the 5/10Å ratio and the
426 crystallinity of illite of potential illite sources from the database of Petschick et al. (1996)
427 (figure 4). This comparison demonstrates that the illite from core MD07-3076Q is similar to
428 illite from the Weddell and Scotia seas while the chemical and crystallographic properties of
429 the illite recovered at site MD07-3076Q is not compatible with a Namibian source. In the
430 Scotia Sea, illite represents less than 30% of the total clay mineral fraction (from 10-30%;
431 Petschick et al., 1996) and represents a mix of illite coming from the Weddell Sea embayment
432 via the AABW, and illite from the Pacific sector of Antarctica delivered by the CDW
433 (Diekmann et al., 2000; Walter et al., 2000; Petschick et al., 1996). Importantly, in the
434 Weddell Sea, illite represents at least 50% of the total clay mineral fraction (more than 80% in
435 some areas; Petschick et al., 1996). Consequently, the Weddell Sea embayment is considered
436 as the major, source of illite for our studied site.

437 Smectite has several potential provenances: the Angola Basin, southern South
438 America, Scotia Sea Islands, and Antarctic Peninsula. The crystallinity of this mineral was
439 measured in order to decipher its provenance. The well-crystallized smectite (low
440 crystallinity; figure 3) is compatible with a provenance from southern South America
441 (Pampas and Patagonia), Scotia Arc, or Antarctic Peninsula, which are all characterized by
442 crystallinity lower than 1.5 (Petschick et al., 1996; figure 3). It rules out a contribution of
443 poorly crystallized smectite (crystallinity > 2; Petschick et al., 1996) from Angola. In detail,
444 the crystallinity of the smectite from our studied site likely corresponds to a mix between two
445 types of sources: (1) Patagonia and Antarctic Peninsula with a crystallinity of 1.5; and (2)

446 Scotia Arc with a crystallinity lower than 1.0. Interestingly, the proportion and crystallinity of
447 smectite record very similar variations that suggest a dominant and rather continuous flux of
448 smectite from the Scotia Arc (low crystallinity - ~1.1) during the last glacial period, with a
449 supplementary supply of less well crystallized smectite (slightly higher crystallinity – 1.5;
450 ~20%) from Patagonia or Antarctic Peninsula during the deglaciation (supplementary figures
451 S1 and S2)

452 In summary, both the proportions of the clay minerals and their crystallographic
453 properties suggest that kaolinite mainly derives from low latitude areas, chlorite originates
454 from Antarctica and the Scotia Sea, while illite mainly derives from the Weddell Sea
455 embayment and smectite is derived from several sources (Scotia Arc, Patagonia, and
456 Antarctic Peninsula). Moreover, mineralogical and crystallographic properties exclude Africa
457 as a source of clay minerals consistent with the dominant westward oceanic circulation in the
458 ACC (figure 1).

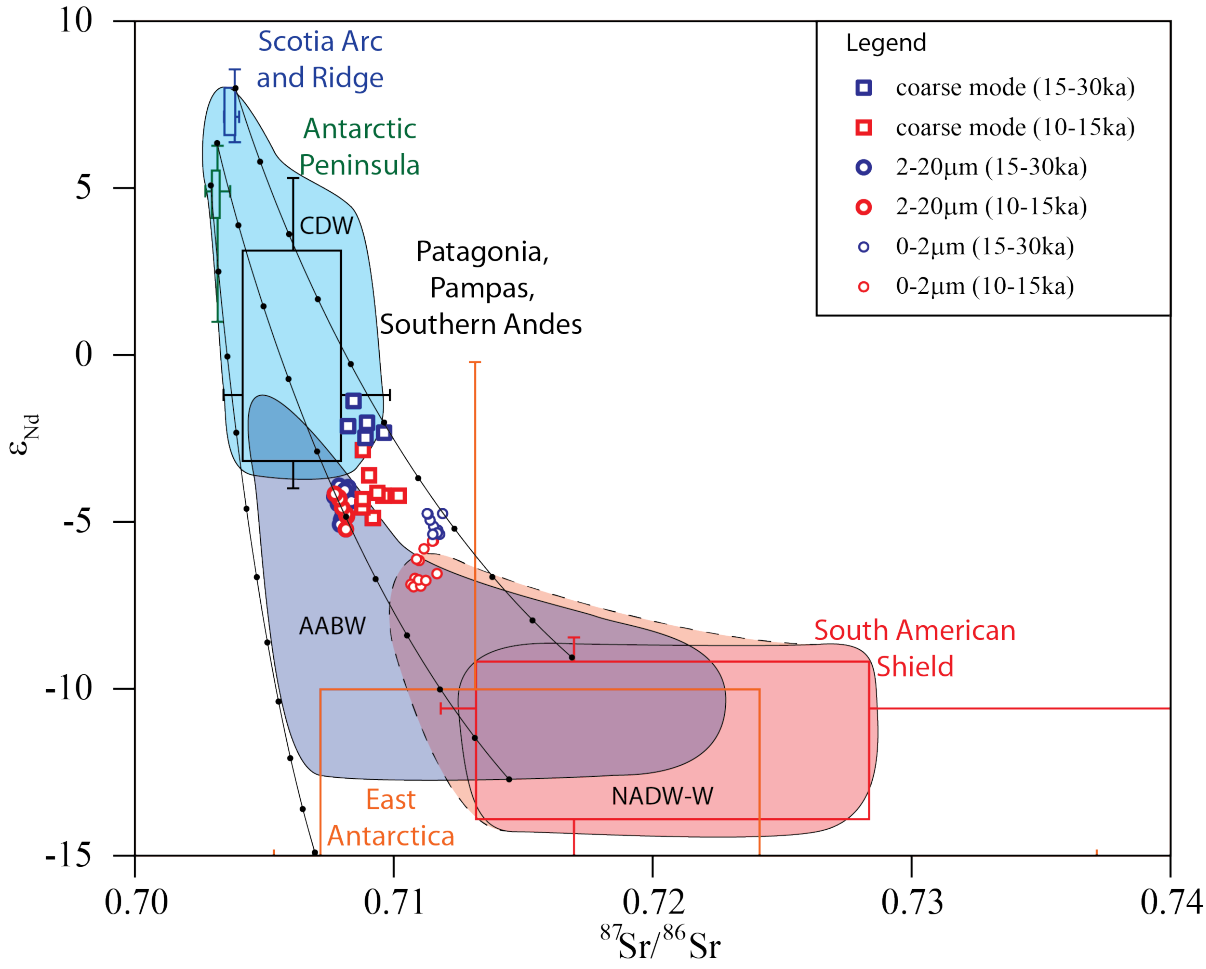

459

460 *Figure 6:* $^{87}Sr/^{86}Sr$-ε_{Nd} *diagram of MD07-3076Q sediments and of potential sources of*
461 *sediments for the South Atlantic Basin. Boxes representing the reference data delimit the first*
462 *and the third quartile. The median values are represented by horizontal and vertical lines*
463 *attached to the boxes for the* ε_{Nd} *and the* $^{87}Sr/^{86}Sr$ *ratios, respectively. The short strokes at the*
464 *end of these lines represent the* 10^{th} *and* 90^{th} *percentile values. Accordingly, the box represent*
465 *50% of values found for each potential provenance, and 80% is represented with the lines.*
466 *Data sources: -South American Shield- Allegre et al. (1996); Basile et al. (1997); Walter et*
467 *al. (2000); de Mahiques (2008); Jeandel et al. (2007), and references therein; Mallmann et*
468 *al. (2007); Ganade de Araujo et al. (2014); Fuck et al. (2014); -Patagonia, Pampas, Southern*
469 *Andes- Stern et al. (1990); Grousset et al. (1992); Basile et al. (1997); Walter et al. (2000);*
470 *Smith et al. (2003); Jeandel et al. (2007), and references therein; Khondoker et al. (2018); -*
471 *Scotia Arc and Ridge- Jeandel et al. (2007); Harrison et al. (2003);-Antarctic Peninsula-*

Hole el al. (1993); Kosler et al. (2009); Roy et al. (2007); Lee et al. (2005); *-East Antarctica-* *DePaolo et al. (1982); Luttinen et al. (1998, 2010); Roy et al. (2007); Will et al. (2010).*

The coupled ε_{Nd} - $^{87}Sr/^{86}Sr$ isotope variation of the clay-size fraction (figure 6) reveal a mixed provenance between young sources around the Scotia Sea (Scotia Arc, Antarctic Peninsula, Patagonia) and southern South America (Patagonia and Pampas), and an old source from East Antarctica or the South American Shield (i.e., Brazil and Parana River).

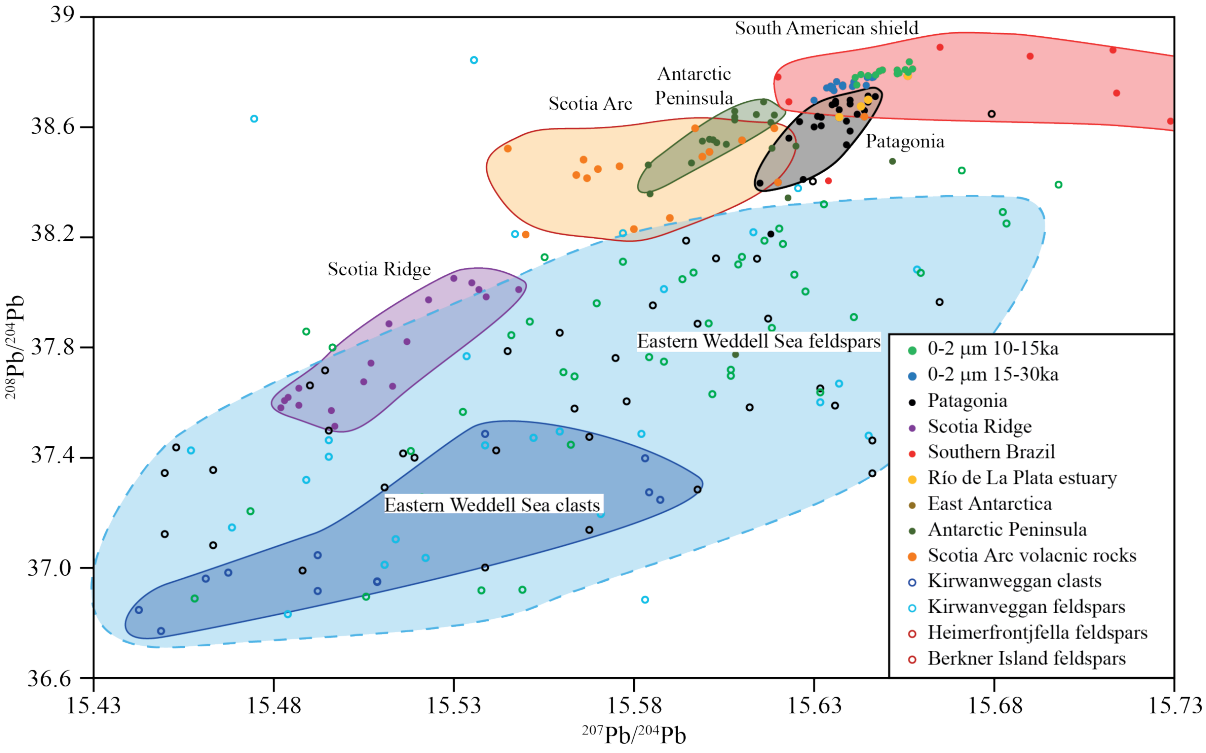

Figure 7: Pb isotope composition of core MD07-3076Q and of potential sources of sediments. The reference data used for comparison are from Fretzdorff et al. (2002), -Scotia Ridge-; Khondoker et al. (2018), -Patagonia-; Cohen and O'Nions (1982); Barreiro (1983), -Scotia Arc-; Lee et al. (2005), Kosler et al. (2009), Flowerdew et al. (2012) -Antarctic Peninsula-, de Mahiques et al. (2007), -South American Shield-; Flowerdew et al., (2012), -Eastern Weddell Sea-.

The coherent Pb isotope variations in figure 7 support this interpretation recording a mix between the Antarctic Peninsula, Scotia Arc, and South American Shield. However, since

very few data are available for the Pb isotope compositions of East Antarctica, a contribution from this area cannot be excluded. The three isotopic systems suggest an increased contribution of older material during the deglaciation compared with the LGM. Based solely on Nd and Pb isotope data, it is rather difficult to distinguish South America and East Antarctica as the old end-members during the deglaciation. However, the increase of the K/C ratio during the deglaciation supports the hypothesis of enhanced relative contribution from the South American Shield.

2. Cohesive silt mode fraction (2-20 μm)

Both $^{87}Sr/^{86}Sr$ and ε_{Nd} of the cohesive silt mode fraction record limited variation throughout the deglaciation (figure 5). The isotopic results indicate that the provenance is located in Patagonia and in the Antarctic Peninsula, with an additional contribution of old source (South American Shield and/or East Antarctica). These results suggest that no major modification of provenance occurred during the deglaciation. Strontium and Nd isotope ratios do not allow discrimination of the source of old material for the cohesive silt mode fraction. The Nd isotope ratios suggest on average a higher radiogenic contribution for cohesive silts compared with the clay-size fraction (figure 6).

3. Sortable silt mode fraction (20-32/40 μm)

Both Sr and Nd isotope ratios of the sortable silt during the LGM record one dominant provenance: the Scotia Sea area (Patagonia, Scotia Arc, Antarctic Peninsula; figure 5). During the deglaciation, an important shift to less radiogenic ε_{Nd} values (4 units) is observed implying an increased contribution of an older end-member such as East Antarctica and/or the South American Shield. However, because East Antarctica and the South American shield have similar Sr and Nd isotope composition, it is not possible to distinguish them with these isotopes (figure 6). Consequently, investigating the main transportation patterns is necessary

511 to identify the source of old material for both the cohesive (2-20 μm) and the sortable silt
512 mode fractions (20-32/40 μm).

513 In summary, (figure 6) all three grain-size fractions compositions are located between
514 two end-members: the Scotia Sea-southern South America area (Antarctic Peninsula, Scotia
515 Arc and Ridge, Patagonia, Pampas, Southern Andes), and crustal shields (East Antarctica,
516 South American Shield). The clay-size fraction appears the most crustal-like, whereas the
517 sortable silt mode presents the most mantle-like composition. The 2-20 μm grain-size fraction
518 presents the lowest $^{87}Sr/^{86}Sr$, meaning that the difference with the other grain size fraction is
519 related to distinct provenances rather than grain size effect. Both the clay size and the sortable
520 silt mode fractions display an increase of the crustal end-member. In the clay size fraction,
521 clay mineralogy enabled the identification of this old crustal source (i.e., the South American
522 Shield).

523 ## B. Transportation pattern and palaeoclimatic implications

524 The provenances of the sediments for the three distinct grain-size fractions have been
525 identified (or partially identified) in the previous section using their mineralogical and
526 geochemical characteristics. Now, we will focus on identifying their transportation patterns
527 and vectors from the source to the sedimentation site.

528 Several studies propose that aeolian processes may lead to significant particle transfers
529 from Patagonia into the central Atlantic sector of the Southern Ocean (Hegner et al., 2007;
530 Desiage et al., 2018). The aeolian contribution of loess from Patagonia was enhanced during
531 the LGM as far as Antarctica (Petit et al., 1990; Grousset et al., 1992; Diekmann, 2007;
532 Lambert et al., 2008). Although this hypothesis could be supported by the radiogenic Nd
533 signal observed in both the clay-size and the sortable silt mode fraction during the LGM, the
534 mineralogical of MD07-3076Q sediments is not in agreement with an enhanced contribution

535 from Patagonia. The dominant clay mineral in Patagonia is smectite (up to 95%), and the
536 contribution of Patagonian smectite in our clay-size fraction is lowest during the LGM (figure
537 3). Consequently, direct aeolian inputs cannot be significant at our site, and oceanic currents
538 appear to be the main contributors to sedimentation (Moriarty, 1977; Petschick et al., 1996;
539 Kuhn and Diekmann, 2002). This means that any aeolian particles from Patagonia delivered
540 to the southwest Atlantic (Mathias et al., 2014) likely reach our site via oceanic transport
541 processes.

542 The size of particles transported by water flow is directly related to the flow energy,
543 with size increasing with the flow speed. This property was used in previous studies to track
544 the temporal evolution of paleo-current flow (e.g. McCave and Hall, 2006; McCave and
545 Andrews, 2019). Below we show that the different grain-size modes not only correspond to
546 distinct flow speeds, but specific water mass at site MD07-3076Q. Consequently, grain-size
547 modes (2-20 μm and 20-32/40 μm) can be associated to specific deep-water-masses.

548 The clay-size fraction (i.e., the < 2 μm particles) with very high specific surface
549 readily floats and hence can undergo long-range transportation (>500 km). Consequently,
550 particles within this grain-size fraction can be used to record the relative contribution of the
551 main deep-water masses.

552 ### 1. Clay-size fraction: the distant terrigenous signal

553 The NADW carries fine suspended particles from as far as the Labrador Sea.
554 However, this signal is probably overprinted by the supply of sediments from more proximal
555 sources such as Africa or South America. The western branch of the NADW (NADW-W; i.e.,
556 Deep Western Boundary Current) can transport sediments from Brazil, Parana River, Pampas,
557 and Patagonia (figure 1). Both mineralogical and geochemical compositions of the particles
558 transported by the western branch of the NADW are likely controlled by the southern
559 extension of the water-mass. Currently the western branch drifts away from the South

560 American coast around 45°S. This southern extension likely changed during the last glacial
561 period and deglaciation (Skinner et al., 2010, 2014; Vasquez-Riveiros et al., 2010;
562 Waelbroeck et al., 2011; Gottschalk et al., 2015a,b; Howe et al., 2016). Depending on its
563 southern extent, the NADW is thus able to carry either mostly kaolinite (equatorial Brazil), or
564 kaolinite and smectite (southern Brazil), or illite (Parana River basin), or well-crystallized
565 smectite (crystallinity ~1.5; Patagonia). As shown above, the ε_{Nd} signature of these sediments
566 is more radiogenic when the NADW extends further south (-20 in equatorial Brazil, to ~0 in
567 Patagonia) while the Pb and Sr yield a slightly less radiogenic signature (figures 6 and 7).

568 The CDW transports sediments from the Scotia Sea area, including Scotia Arc,
569 Patagonia, and the Antarctic Peninsula, as well as from the Weddell Sea when mixing occurs
570 between the lower part of the LCDW and AABW. Then particles transported by the CDW
571 likely record a younger isotopic signature (i.e., more radiogenic ε_{Nd} and unradiogenic Sr and
572 Pb isotopes), and a mineralogical composition dominated by smectite and chlorite, while
573 additional contribution of old material (unradiogenic ε_{Nd} and radiogenic Sr and Pb isotopes)
574 and illite is possible when the LCDW and AABW mix together. In summary, illite is
575 considered as injected into the sedimentary system via the AABW through mixing processes
576 between LCDW and AABW while smectite and chlorite are likely transported by the CDW.

577 The AABW in the Atlantic sector mainly forms in the Weddell Sea embayment (Orsi
578 et al., 1999), and thus, must carries sediments from its drainage basin (East Antarctica,
579 Antarctic Peninsula), but may also transport sediment winnowed on its pathway such as the
580 Scotia Arc or southern Patagonia in the Argentine Basin. The main clay minerals in the
581 Weddell Sea embayment are illite associated with chlorite. Smectite may be injected in the
582 AABW at the vicinity of the Scotia Arc. Kaolinite is almost absent in both the Weddell Sea
583 embayment and the Scotia Sea area (Patagonia, Antarctic Peninsula and Scotia Arc) and is
584 unlikely to be transported by the AABW. The isotopic composition of fine particles

585 transported by the AABW ranges between two end-members: the very old sediments from
586 East Antarctica ($^{87}Sr/^{86}Sr > 0.72$; $\varepsilon_{Nd} < -20$), and younger material from the Antarctic
587 Peninsula and the Scotia Arc ($^{87}Sr/^{86}Sr \sim 0.70$; $\varepsilon_{Nd} > -5$; intermediate Pb isotope ratios).
588 Consequently, the composition of particles transported by the AABW flowing out of the
589 Weddell Sea is intermediate, with ε_{Nd} around -9 (Walter et al., 2000), and is potentially
590 enriched in young material when entering the Scotia Sea.

591 The above observations are summarized in table 5, in which specific isotopic and
592 mineralogical signatures are associated to each deep water mass. It is clear that the K/C ratio
593 as well as the ε_{Nd} composition reflect northern- versus southern-born water mass contributions
594 (i.e., NADW versus CDW and AABW). Similarly, smectite and illite are transported by
595 distinct water-masses and the illite/smectite ratio (I/S) can efficiently distinguish the AABW
596 from the other water-masses. Thus, this ratio will further be used as a tool for estimating the
597 AABW contribution through time.

598 The illite/smectite and kaolinite/smectite ratios have been plotted in figure 8. The three
599 end-members for AABW, CDW and NADW are plotted according to the clay composition of
600 their suspended loads. Figure 8 highlights how the relative contribution of the three water
601 masses (i.e., AABW, CDW, and NADW) to clay deposition has changed with time since the
602 LGM. To interpret this figure it is important to keep in mind that changes observed in the
603 contribution one deep water mass are relative compared to the other water masses. To
604 construct figure 8.b, the proportion of clay particles deposited by each deep water mass was
605 calculated as described below.

606 End-member deep water mass compositions were calculated from the average
607 composition of deep water-masses shown in figure 8.a. Weights are computed as the inverse
608 of the distance between the position of water-mass end-member (x_w;y_w) with $x_w = K/C_w$ and

609 $y_w=I/S_w$ and the position of the data point $(x_d;y_d)$, with $x_d=K/C_d$ and $y_d=I/S_d$ taken from the
610 graph (figure 8.a) for each water-mass: $W_w=1/[\ (x_d-xw)^2+(y_d-y_w)^2]^{1/2}$. The position used for
611 the deep water masses are: $xA_{ABW} = K/C_{AABW} = 0.3$; $y_{AABW} = I/S_{AABW} = 2.5$; $x_{CDW} = K/C_{CDW}$
612 $= 0.1$; $y_{CDW} = I/S_{CDW} = 1$; $x_{NADW} = K/C_{NADW} = 0.9$; $y_{NADW} = I/S_{NADW} = 1$. The values used
613 for the NADW correspond to the mineralogical composition of the NADW during the LGM.
614 As a result, the contribution of NADW to the deposition of clay particles is underestimated
615 (~10%) at the end of the deglaciation while the contribution of the CDW is overestimated
616 (~10%). This choice does not have a strong impact on the contribution of the AABW (less
617 than 4.5%). Second, the percentage of the contribution of each water mass is calculated by
618 bringing the sum of the weights computed to 100: [NADW's contribution] = $W_{NADW}/(W_{NADW}$
619 $+ W_{CDW} + W_{AABW}) \times 100$

620 To test the validity of this method to reconstruct the evolution of the past deep
621 circulation, we compared our results with those of other water-masses proxies (e.g. seawater
622 ε_{Nd} and $\delta^{13}C$). However, these latter methods proved incapable of distinguishing AABW from
623 CDW. Consequently, we based the comparison on the proportion of the NADW compared to
624 the southern sourced deep waters. Based on data from the same core, our estimates give
625 comparable results to these two proxies (see table 6). This suggests that our approach
626 successfully reconstructs the evolution of these three deep water masses. However, our
627 estimate of the proportion of the NADW is higher than the estimate of Howe et al. (2016)
628 based on ε_{Nd}. This discrepancy can be explained by two factors. First, we were unable to
629 make corrections for concentration differences of particles in the three deep water masses
630 (i.e., quantity of clay particles per volume of water) due to the large uncertainties involved. In
631 addition, it is very likely that the NADW is more concentrated in clay particles than the
632 AABW and CDW due to sediment source effect (e.g., dry East Antarctica below thick ice
633 sheets vs. humid South America highly drained by equatorial rivers). Consequently, even

though our tool successfully reconstruct the variations of the NADW, the contribution of NADW is probably overestimated. In other words, our estimate of NADW contribution to the clay deposition is likely higher than the proportion of NADW (in volume of water). Second, the choice of the end member for the seawater ε_{Nd} of AABW+CDW made by Howe et al. (2016) is debatable (-5.5 during the LGM, -8.5 during the Holocene). Skinner et al. (2013) used a compositional end-member between -5 and -2, which yields a better match with the isotopic composition of seawater Nd at our site (-5.5, Skinner et al., 2013). Therefore, the estimate of Howe et al. (2016) appears to underestimate the contribution of NADW at our site.

From 25 to 20 ka, the CDW is clearly dominant, with a contribution of 50% on average, while the NADW and AABW deliver 35% and 15% of the clay fraction, respectively. The highest contribution of the AABW is observed at the end of the LGM between 20 and 17.5 ka (27% in average, but up to 52% at 18 ka). During this interval, the NADW and CDW deliver respectively 34% and 39% on average. At the end of this period, the mineralogical composition of the fine sediments deposited at site MD07-3076Q suggests that the AABW was dominant. At the beginning of the deglaciation, between 17.5 and 15 ka (i.e., during HS 1), the clay mineral composition of core MD07-3076Q indicates a decreased relative contribution of the AABW end-member (15% on average) associated to an increase of the relative contribution of the CDW (49%) end-member. This observation of an increase of the CDW contribution is supported by the radiogenic ε_{Nd} of the clay-size fraction and a $^{87}Sr/^{86}Sr$ close to the Scotia Arc composition (figures 5 and 6).

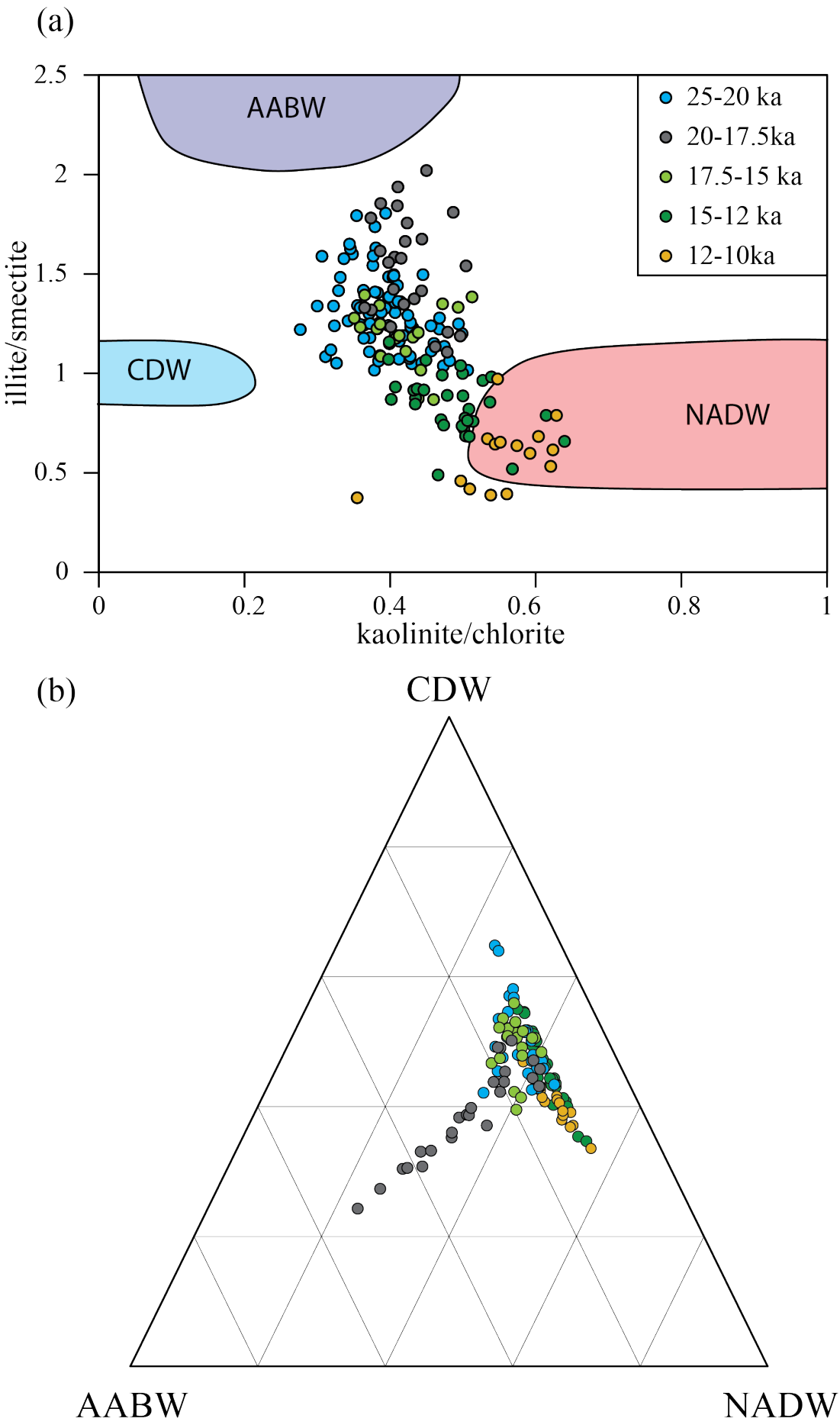
(a)
AABW
CDW
NADW
25-20 ka
20-17.5ka
17.5-15 ka
15-12 ka
12-10ka
illite/smectite
kaolinite/chlorite
0
0.5
1
1.5
2
2.5
0.2
0.4
0.6
0.8
(b)
CDW
AABW
NADW

655

Figure 8: (a) Plot of kaolinite/chlorite vs illite/smectite ratios from core MD07-3076Q from 25 to 10 ka. The composition of deep-water masses has been determined using the data from Petschick et al. (1996). (b) Ternary diagram comparing the contribution of the three deep water masses to the clay deposition at site MD07-3076Q.

From 15 ka on, the clay mineral composition at the study site records an increasing contribution of the NADW until the end of the deglaciation (at least 47% for the interval 10-12 ka, figure 8). Compared with the LGM this suggests enhanced contribution of the NADW with reduced contributions from the CDW (40% for the interval 10-12 ka) and AABW (13% for the interval 10-12 ka). These results are strongly supported by the sharp decrease in ε_{Nd} and by the concomitant increase of $^{208}Pb/^{204}Pb$ and $^{207}Pb/^{204}Pb$ ratios from the clay size fraction (figures 5 and 7). This corroborates the conclusions based on the *cibicides* $\delta^{13}C$ measured in the same core (figure 9.e, Waelbroeck et al., 2011). In addition, increasing inputs of less crystallized smectite (slightly higher crystallinity: ~1.5, supplementary figure S1) from Patagonia support the southward penetration of the NADW in the southern Atlantic Ocean, consistent with an increasing contribution of the NADW-W to sedimentation at site MD07-3076Q. Interestingly, the transition between B/A (that starts simultaneously with the southern Hemisphere cooling, the Antarctic Cold Reversal) and the YD appears to have no effect on the relative contribution of deep water masses and shows a continuous increase of the relative contribution of the NADW during these two periods.

Overall, the clay size fraction demonstrates that the contribution of the three deep water-masses changed through time. An increase of contribution of the AABW is recorded at the end of the LGM and is followed by a two-step deglaciation. First, an important reduction of the AABW is observed at the HS 1 onset. Second, an increase in the NADW contribution compared to the CDW is observed during the B/A and YD.

2. Cohesive silt mode fraction (2-20 μm): an AABW signal

According to our geochemical data, the provenance of the cohesive silt fraction is dominated by sources from the Scotia Sea area, especially Patagonia and Antarctic Peninsula, and by an old, unidentified, crustal source. According to the modern deep oceanic circulation, only the CDW and AABW are able to transport sediment from the Scotia Sea to the studied site (figure 1). It was also likely the case during the LGM and deglaciation. The AABW and CDW were likely spreading further north while the NADW was likely shallower, and retreated to the north (Kuhn and Diekmann, 2002; Barker et al., 2010; Waelbroeck et al., 2011). These modifications do not affect the continental sources of terrigeneous sediment for the CDW and AABW compared the present day, and the NADW is still unable to transport sediments from the Scotia Sea. Consequently, it excludes the NADW as a transport medium for the cohesive silt mode fraction to site MD07-3076Q. Therefore, because the NADW is also the only water-mass able to transport sediment from the South American Shield to our study site, it excludes the South American Shield as a source of sediment for the cohesive silt mode fraction, and implies East Antarctica as the source of old material identified in the cohesive silt mode fraction. The terrigenous supplies deriving from East Antarctica/Scotia Sea strongly suggest the AABW has been the dominant carrier of the 2-20 μm grain-size fraction since the LGM. In addition, because the mean isotopic composition of this grain-size fraction transported by the AABW is relatively constant through time (figure 6), the relative contributions of East Antarctica and Scotia Sea area seem to have remained largely unchanged since the LGM.

3. Sortable silt mode fraction (20-32/40 μm): A LCDW signal

A part of the particles transported by the AABW and the NADW are derived from old crustal sources (i.e., East Antarctica and South American Shield, respectively). Thence, these two deep-water masses cannot be the source of the sortable silt mode fraction during the

LGM. In contrast, the CDW is a good candidate to transport particles solely from the Scotia Sea, as identified for the sortable silt mode fraction during the LGM. Consequently, the only possible source of this grain size fraction is the CDW. During the deglaciation, the Nd isotope composition of the sortable silt mode fraction became gradually less radiogenic while the $^{87}Sr/^{86}Sr$ ratio fluctuated, suggesting a modification of provenances and/or an additional contribution of less radiogenic Nd source. Such isotopic changes could be explained in two ways; (1) a change in the CDW pathway; (2) the incorporation of terrigenous material by mixing with other water-masses (such as AABW or NADW). The CDW slowed down and migrated southward during the deglaciation in concert with the southward migration of the subpolar and polar fronts (Howard and Prell, 1992; Anderson et al., 2009; Denton et al., 2010). However, such a change in the CDW pathway would have no effect on the terrigenous sources of particles. In contrast, several studies proposed increased ventilation in the Southern Ocean, enabling the degassing of oceanic CO_2 to the atmosphere (Ahn and Brook, 2008; Fischer et al., 2010; Skinner et al., 2010, 2013, 2014; Siani et al., 2013). Currently the base of the LCDW is mixed with the AABW, which was apparently not the case during the LGM (Skinner et al., 2010). The onset of AABW/LCDM mixing could explain the incorporation of unradiogenic terrigenous material from the Weddell Sea embayment (i.e., East Antarctica) into the LCDW. This mechanism likely explains the shift in ε_{Nd} composition during the deglaciation. This hypothesis is supported by the results of Walter et al. (2000) who reported lower ε_{Nd} in terrigenous sediments in the southern Scotia Sea during the interglacial period and interpreted this as higher contribution of sediment from the Weddell Sea embayment due to the mixing of the AABW into the ACC. From 15 ka, the Nd isotope composition of the sortable silt mode fraction is very close to the one from the cohesive silt mode fraction transported by the AABW. It suggests that the sortable silt mode fraction is specifically transported by the LCDW rather than by the entire CDW. This highlights the fact that the ε_{Nd}

variations from the sortable silt mode fraction provide a useful tool to study the mixing between the AABW and LCDW.

Figure 9 AD1

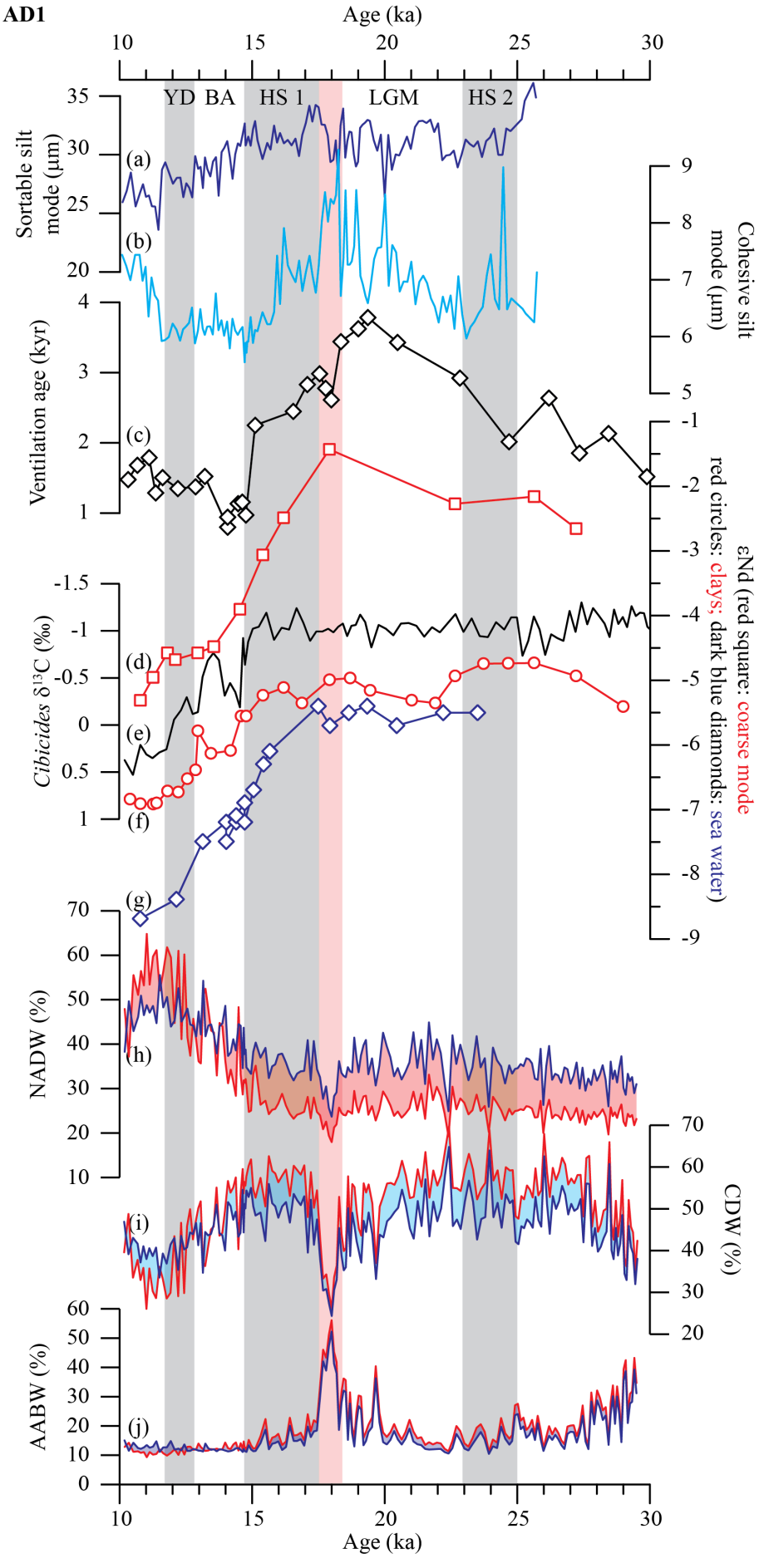

732

Figure 9: Comparison between paleoceanographic proxies from core MD07-3076Q and data produced in this study. Grey areas delimit the main climatic events and the red band highlights the particularly strong AABW event. (a) size of the sortable silt mode (μm), a proxy of the speed of the LCDW; (b) size of the cohesive silt mode (μm), a proxy of the speed of the AABW; (c) bottom water ventilation age from site MD07-3076Q (data from Skinner et al., 2010); (d) ε_{Nd} from the sortable silt size fraction; (e) Cibicides $\delta^{13}C$ from site MD07-3076Q (Waelbroeck et al., 2011); (f) ε_{Nd} from the cohesive silt size fraction; (g) seawater ε_{Nd} from site MD07-3076Q (Skinner et al., 2013); (h) proportion of clay particles delivered by the NADW (see figure 8.b); (i) proportion of clay particles delivered by the CDW (see figure 8.b); (j) proportion of clay particles delivered by the AABW (see figure 8.b). On curves (h), (i) and (j), the red line represent values calculated using the Holocene end-member of the NADW (I/S = 0.5), while the blue line correspond to the values calculated using the LGM end-member of the NADW (I/S = 1).

4. Paleoceanographic implication

Our results establish that different grain-size modes can be attributed to distinct water-masses and that variation of the particle size of the different grain-size modes (figure 2) can be used to record the variations of flow speed of these water-masses as well as changes in pathways/mixing. This method has the advantage of distinguishing the speed of each water mass instead of giving the average speed of all the water masses, as it is the case for the sortable silt method (McCave and Hall, 2006). During the last glacial period, the large mean particle diameter (>30 μm) of the sortable silt mode fraction reflects strong LCDW activity. At the beginning of the deglaciation, the variation of the mean particle size suggests that the LCDW speed slightly decreased, but remained high. Since ~15 ka, the LCDW speed has been showing a gradual decrease. McCave et al. (2014) observed minor change in the Antarctic Circumpolar Current (which includes the CDW) flow speed at the Drake Passage during the

758 deglaciation. Our observation, however, is consistent with other studies in the south Indian
759 sector of the Southern Ocean indicating that the Antarctic Circumpolar Current (which
760 includes the CDW) flow speed was maximum during the LGM and decreased during the
761 deglaciation (Mazaud et al., 2010), with a notable increase from ~15 ka on (Mazaud et al., in
762 prep.). Altogether, these studies and our results suggest that the weakening of the ACC started
763 at ~15 ka.

764 From ~26 to 21 ka, the low particle sizes recorded in the cohesive silt mode (figure
765 2.b, transported by the AABW) indicate slow AABW, which is consistent with the observed
766 moderate relative contribution of AABW in clay particles (figure 8 and 9). In this time
767 interval, one isolated high value is recorded at 24 ka and suggests that, temporarily, AABW
768 activity was stronger. However, no change is registered in the clay minerals (figure 3 and 9).
769 The grain-size data indicate that the AABW became more vigorous from 21 ka to reach its
770 strongest speed at the end of the LGM. This maximum speed is concomitant with the
771 strongest relative contribution of the AABW of the clay record (figures 3.h and 9), as shown
772 by the peak of the illite/smectite ratio (figure 3) illustrated on figure 8. Interestingly, this
773 AABW maximum preceded the HS 1, and both its speed and relative contribution fell at the
774 LGM/HS 1 transition as defined by Missiaen et al. (2019). At the beginning of the
775 deglaciation, the abrupt decrease of the fine grain-size mode indicates a slowdown of the
776 AABW (figure 2). This is supported by a sharp decrease in the illite/smectite ratio in the clay-
777 size fraction (figure 3), which also suggests an abrupt decrease of the relative contribution of
778 the AABW. At ~16 ka, a slowdown of the AABW is indicated by a second sharp decrease of
779 the cohesive silt mode (figure 2), which reaches its lowest values of the entire record,
780 indicating low AABW speed from 16 to 11.5 ka, when the AABW activity increased
781 suddenly and recovered the speed observed before 16 ka.

These variations of the AABW speed could indicate the transition from the Ice Shelf Mode dominated bottom water formation at the end of the LGM to the Polynyas Mode dominated bottom water formation during interglacial periods. The variations of the cohesive silt mode support a strong AABW during the LGM and the early Holocene, and a minimum flow during the deglaciation. This minimum flow would result from the reduction of bottom water production via the Ice Shelf Mode and still low production via the Polynyas Mode. Our results confirm the results of Krueger et al. (2012) who demonstrated the relation between the flow speed changes in the Cape Basin and the higher AABW production rates and indicate that the size of the cohesive silt mode is a reliable tracer of the AABW flow speed and hence of AABW production rates in the Weddell Sea.

Overall, the variations of the AABW flow speed and ventilation age are similar, with higher average speeds corresponding to the old ventilation ages. Taken together with the reconstructed vigorous LCDW during the LGM (figure 9.a.), these observations suggest that the deep Southern Ocean was poorly ventilated but with a vigorous circulation. It means that both the AABW and LCDW remained isolated from the surface during the LGM. This conclusion is consistent with our hypothesis that AABW was formed under ice shelves during this period and that the major expansion of sea ice (Bianchi and Gersonde, 2004; Bostock et al., 2012; Adkins 2013) kept the AABW isolated from the atmosphere during the LGM. In addition, poorly ventilated deep Southern Ocean associated with a vigorous deep circulation (i.e., high AABW and LCDW flow) suggests that a barrier existed between the deep ocean and the surface, which is consistent with the study of Howe et al. (2016). In contrast, direct comparison highlights the fact that the peaks of ventilation age and of the AABW flow are not in phase. Indeed, the peaks of the AABW flow (figure 9.b) and of the AABW contribution to clay deposition (figure 9.j) are synchronous with the first decrease in deep water ventilation ages after the LGM and prior to HS1. Moreover, this well-defined change in the AABW

807 behavior is recorded by two distinct proxies (i.e., clay minerals and grain size distribution)
808 and in two distinct grain size fractions (clays and silts). These synchronous changes are
809 associated with a drop in ventilation age prior to the HS 1. The variations in two grain size
810 fractions that are transported and deposited by distinct dynamic processes indicates a major
811 perturbation in Southern Ocean circulation. Interestingly, the increase in the AABW strength
812 associated to the early decrease in deep water ventilation age took place significantly earlier
813 than the changes recorded by the other proxies measured in core MD07-3076Q (i.e., sea water
814 ε_{Nd} between 17.5 and 16 ka, $\delta^{13}C$ at 14.5 ka, $\delta^{18}O$ at 15 ka, LCDW flow speed at 15 ka,
815 NADW proportion at 15 ka) and also precedes the atmospheric CO_2 rise (Bereiter et al., 2015)
816 and the change in the opal flux (Anderson et al., 2009). For the first time, these data indicate a
817 change in the deep Southern Ocean circulation that is associated with ventilation change that
818 precedes the HS 1. This suggest that the identified large temporary (~1 kyr long) increase in
819 the AABW contribution and flow speed may have had a substantial impact on the deep
820 Southern Ocean ventilation, and by extension, on the deglacial CO_2 rise. Indeed, the
821 magnitude of the change in the AABW behavior has the potential to "break" the hypothetical
822 physical barrier between the deep Southern Ocean and the surface that was responsible of
823 poorly ventilated deep water during the LGM. This combination of events also explains the
824 unexpected early fall of the deep water ventilation age observed at ~18.2 ka.

825 ## Conclusion

826 The mineralogical characteristics of the clay-size fraction provide new insights into
827 the general thermohaline circulation in the southern South Atlantic. The mineralogical signal
828 demonstrates strong influence of both the CDW and AABW during the last glacial period.
829 Clay assemblages reveal a particularly high contribution of the AABW at the end of the
830 LGM, which is interpreted as reflecting strong Ice Shelf Mode bottom water production in the
831 Weddell Sea. The contribution of the CDW and AABW then progressively decreases during

832 the deglaciation together with the growing influence of the NADW (figure 8). Indeed, clay
833 size fraction data monitor the progressive incursion of NADW into the Southern Ocean
834 during the deglaciation from ~15 ka (figure 8), as well as the synchronous southward retreat
835 of the southern-born deep water-masses (i.e., CDW and AABW).

836 The isotopic compositions of the distinct grain size modes provides invaluable
837 information. The sortable silt mode fraction helps to trace the LCDW activity whereas the
838 cohesive silt mode fraction is associated with the AABW signal. Consequently, the temporal
839 evolution of flow speeds, pathways and interactions of these deep water-masses can be
840 determined in a very robust way. This study suggests: (1) vigorous LCDW during the LGM
841 and a marked weakening from ~15 ka; (2) strong AABW at the end of the LGM and during
842 the early Holocene, and weak AABW during the deglaciation between 16 and 11.5 ka. These
843 results suggest a decrease of AABW production rates during the deglaciation that could result
844 from the transition from strong Ice Shelf Mode bottom water production during the LGM to
845 stronger Polynyas Mode bottom water during the Holocene.

846 The strong LCDW speed observed during the LGM is associated with increased clay
847 deposition by the CDW, and the reduction of LCDW speed since the B/A is accompanied by
848 an increased clay contribution from the NADW. Similarly, the highest AABW speed recorded
849 at the end of the LGM is concomitant with the highest relative contribution of the AABW to
850 clay mineral deposition. Interestingly, this AABW maximum preceded the HS 1 and both its
851 speed and contribution fell markedly at the LGM/HS 1 transition.

852 Finally, this study demonstrates that based on (1) the combination of isotopic and
853 mineral investigation of the clay size fraction, (2) the combination of isotopic measurement of
854 isolated grain size modes and of grain size distribution results, and (3) a complete synthesis of
855 the potential sources of sediments, it is possible to obtain reliable information on the
856 lithogenic material transported by each deep water mass. This approach allows efficient

tracking of the evolution of distinct water-masses through time, since it helps to isolate the specific signal associated to each water-mass. Based on these observations, we conclude that the increase in the AABW strength at the end of the LGM may have had a substantial impact on the ventilation recovery of the deep Southern Ocean, and by extension, to the deglacial CO_2 rise.

Acknowledgments

We wish to thank Richard Smeets for his invaluable help in the clean lab, Emmeke Bos, Janne Koorneef, and Mathijs van de Ven for the help with TIMS Triton measurements, Bas van der Wagt and Kirsten van Zuilen for Neptune MC-ICPMS measurements. Tristan Lippens is thanked for computer support. We also wish to thank all organizations that provided financial support to the project: the "region Haut de France" and the Vrije Universiteit of Amsterdam. The research was supported by Europlanet 2020 RI, which received funding from the European Union's Horizon 2020 research and innovation programme under grant agreement No 654208. We also want to express our special thanks to the "flotte océanographique française" for retrieving the sediment core used in this study. FB and VBR thanks Monique Gentric for administrative support. CW acknowledges support from the European Research Council ERC grant ACCLIMATE/n° 339108.

References

Adkins, J.F., 2013. The role of deep ocean circulation in setting glacial climates. Paleoceanography 28, 539–561. https://doi.org/10.1002/palo.20046, 2013

Ahn, J., Brook, E.J., 2008. Atmospheric CO2 and Climate on Millennial Time Scales During the Last Glacial Period. Science 322, 83. https://doi.org/10.1126/science.1160832

879 Allègre, C.J., Dupré, B., Négrel, P., Gaillardet, J., 1996. Sr-Nd-Pb isotope systematics in
880 Amazon and Congo River systems: constraints about erosion processes. Chemical
881 Geology 131, 93–112. https://doi.org/10.1016/0009-2541(96)00028-9

882 Anderson, J.J., 1965. Bedrock geology of Antarctica: A summary of exploration, 1831–1962.
883 Geology and Paleontology of the Antarctic 6, 1–70.
884 https://doi.org/10.1029/AR006p0001

885 Anderson, R.F., Ali, S., Bradtmiller, L.I., Nielsen, S.H.H., Fleisher, M.Q., Anderson, B.E.,
886 Burckle, L.H., 2009. Wind-Driven Upwelling in the Southern Ocean and the Deglacial
887 Rise in Atmospheric CO2. Science 323, 1443.
888 https://doi.org/10.1126/science.1167441

889 Barker, S., Diz, P., Vautravers, M.J., Pike, J., Knorr, G., Hall, I.R., Broecker, W.S., 2009.
890 Interhemispheric Atlantic seesaw response during the last deglaciation. Nature 457,
891 1097. https://doi.org/10.1038/nature07770

892 Barker, S., Knorr, G., Vautravers, M.J., Diz, P., Skinner, L.C., 2010. Extreme deepening of
893 the Atlantic overturning circulation during deglaciation. Nature Geoscience 3, 567.
894 https://doi.org/10.1038/ngeo921

895 Barreiro, B., 1983. Lead isotopic compositions of South Sandwich Island volcanic rocks and
896 their bearing on magmagenesis in intra-oceanic island arcs. Geochimica et
897 Cosmochimica Acta 47, 817–822. https://doi.org/10.1016/0016-7037(83)90115-1

898 Barrett, P.J., 1991. The Devonian to Jurassic Beacon Supergroup of the Transantarctic
899 Mountains and correlatives in other parts of Antarctica, in: The Geology of Antarctica.
900 pp. 120–152.

Barros, A.M., Silva, R.D., Cardoso, O.R.F.A., Freire, F.A., Souza Junior, J.J., Rivetti, M., Luz, D.S., Palmeira, R.C.B., Tassinari, C.C.G., 1982. Geologia, BRASIL. Ministério das Minas e Energia. Projeto RADAMBRASIL Folha SD.

Basile, I., Grousset, F.E., Revel, M., Petit, J.R., Biscaye, P.E., Barkov, N.I., 1997. Patagonian origin of glacial dust deposited in East Antarctica (Vostok and Dome C) during glacial stages 2, 4 and 6. Earth and Planetary Science Letters 146, 573–589. https://doi.org/10.1016/S0012-821X(96)00255-5

Bayon, G., Burton, K.W., Soulet, G., Vigier, N., Dennielou, B., Etoubleau, J., Ponzevera, E., German, C.R., Nesbitt, R.W., 2009. Hf and Nd isotopes in marine sediments: Constraints on global silicate weathering. Earth and Planetary Science Letters 277, 318–326. https://doi.org/10.1016/j.epsl.2008.10.028

Bayon, G., Skonieczny, C., Delvigne, C., Toucanne, S., Bermell, S., Ponzevera, E., André, L., 2016. Environmental Hf–Nd isotopic decoupling in World river clays. Earth and Planetary Science Letters 438, 25–36. https://doi.org/10.1016/j.epsl.2016.01.010

Bayon, G., Toucanne, S., Skonieczny, C., André, L., Bermell, S., Cheron, S., Dennielou, B., Etoubleau, J., Freslon, N., Gauchery, T., Germain, Y., Jorry, S.J., Ménot, G., Monin, L., Ponzevera, E., Rouget, M.-L., Tachikawa, K., Barrat, J.A., 2015. Rare earth elements and neodymium isotopes in world river sediments revisited. Geochimica et Cosmochimica Acta 170, 17–38. https://doi.org/10.1016/j.gca.2015.08.001

Beny, F., Toucanne, S., Skonieczny, C., Bayon, G., Ziegler, M., 2018. Geochemical provenance of sediments from the northern East China Sea document a gradual migration of the Asian Monsoon belt over the past 400,000 years. Quaternary Science Reviews 190, 161–175. https://doi.org/10.1016/j.quascirev.2018.04.032

924 Bereiter, B., Eggleston, S., Schmitt, J., Nehrbass□Ahles, C., Stocker, T.F., Fischer, H.,
925 Kipfstuhl, S., Chappellaz, J., 2015. Revision of the EPICA Dome C CO2 record from
926 800 to 600 kyr before present. Geophysical Research Letters 42, 542–549.
927 https://doi.org/10.1002/2014GL061957

928 Bianchi, C., Gersonde, R., 2004. Climate evolution at the last deglaciation: the role of the
929 Southern Ocean. Earth and Planetary Science Letters 228, 407–424.
930 https://doi.org/10.1016/j.epsl.2004.10.003

931 Bostock, H.C., Barrows, T.T., Carter, L., Chase, Z., Cortese, G., Dunbar, G.B., Ellwood, M.,
932 Hayward, B., Howard, W., Neil, H.L., Noble, T.L., Mackintosh, A., Moss, P.T., Moy,
933 A.D., White, D., Williams, M.J.M., Armand, L.K., 2013. A review of the Australian–
934 New Zealand sector of the Southern Ocean over the last 30 ka (Aus-INTIMATE
935 project). Quaternary Science Reviews 74, 35–57.
936 https://doi.org/10.1016/j.quascirev.2012.07.018

937 Bouttes, N., Paillard, D., Roche, D.M., Waelbroeck, C., Kageyama, M., Lourantou, A.,
938 Michel, E., Bopp, L., 2012. Impact of oceanic processes on the carbon cycle during
939 the last termination. Climate of the Past 8, 149–170. https://doi.org/10.5194/CP-8-149-
940 2012

941 Bremner, J.M., Willis, J.P., 1993. Mineralogy and geochemistry of the clay fraction of
942 sediments from the Namibian continental margin and the adjacent hinterland. Marine
943 Geology 115, 85–116. https://doi.org/10.1016/0025-3227(93)90076-8

944 Brown, G., 1980. X-ray diffraction procedures for clay mineral identification. Crystal
945 structures of clay minerals and their X-ray identification 305–359.

946 Burke, A., Robinson, L.F., 2012. The Southern Ocean's Role in Carbon Exchange During the
947 Last Deglaciation. Science 335, 557–561. https://doi.org/10.1126/science.1208163

948 Campodonico, V.A., García, M.G., Pasquini, A.I., 2016. The geochemical signature of
949 suspended sediments in the Parana River basin: Implications for provenance,
950 weathering and sedimentary recycling. CATENA 143, 201–214.
951 https://doi.org/10.1016/j.catena.2016.04.008

952 Capurro, L.R., 1955. Expedición argentina al Mar de Weddell, diciembre de 1954 a enero de
953 1955. República Argentina, Ministerio de Marina, Dirección General de Navegación.

954 Clapperton, C.M., 1993. Quaternary geology and geomorphology of South America. Elsevier
955 Amsterdam etc.

956 Cohen, R.S., O'Nions, R.K., 1982. Identification of recycled continental material in the
957 mantle from Sr, Nd and Pb isotope investigations. Earth and Planetary Science Letters
958 61, 73–84. https://doi.org/10.1016/0012-821X(82)90040-1

959 Cordani, U.G., Sato, K., 1999. Crustal evolution of the South American Platform, based on
960 Nd isotopic systematics on granitoid rocks. Episodes-Newsmagazine of the
961 International Union of Geological Sciences 22, 167–173.

962 Curry, W.B., Oppo, D.W., 2005. Glacial water mass geometry and the distribution of δ13C of
963 ΣCO2 in the western Atlantic Ocean. Paleoceanography 20.
964 https://doi.org/10.1029/2004PA001021

965 de Alkmim, F.F., 2015. Geological Background: A Tectonic Panorama of Brazil, in: Vieira,
966 B.C., Salgado, A.A.R., Santos, L.J.C. (Eds.), Landscapes and Landforms of Brazil.
967 Springer Netherlands, Dordrecht, pp. 9–17. https://doi.org/10.1007/978-94-017-8023-
968 0_2

969 de Almeida, F.F.M., Hasui, Y., de Brito Neves, B.B., Fuck, R.A., 1981. Brazilian structural
970 provinces: An introduction. Earth-Science Reviews 17, 1–29.
971 https://doi.org/10.1016/0012-8252(81)90003-9

de Mahiques, M.M., Tassinari, C.C.G., Marcolini, S., Violante, R.A., Figueira, R.C.L., da Silveira, I.C.A., Burone, L., de Mello e Sousa, S.H., 2008. Nd and Pb isotope signatures on the Southeastern South American upper margin: Implications for sediment transport and source rocks. Marine Geology 250, 51–63. https://doi.org/10.1016/j.margeo.2007.11.007

D'el-Rey Silva, L.J.H., Walde, D.H.-G., Saldanha, D.O., 2016. The Neoproterozoic–Cambrian Paraguay Belt, central Brazil: Part I — New structural data and a new approach on the regional implications. Tectonophysics 676, 20–41. https://doi.org/10.1016/j.tecto.2016.03.019

Denton, G.H., Anderson, R.F., Toggweiler, J.R., Edwards, R.L., Schaefer, J.M., Putnam, A.E., 2010. The Last Glacial Termination. Science 328, 1652. https://doi.org/10.1126/science.1184119

DePaolo, D.J., Manton, W.I., Grew, E.S., Halpern, M., 1982. Sm–Nd, Rb–Sr and U–Th–Pb systematics of granulite facies rocks from Fyfe Hills, Enderby Land, Antarctica. Nature 298, 614–618. https://doi.org/10.1038/298614a0

Desiage, P.-A., Montero-Serrano, J.-C., St-Onge, G., Crespi-Abril, A.C., Giarratano, E., Gil, M.N., Haller, M.J., 2018. Quantifying sources and transport pathways of surface sediments in the Gulf of San Jorge, central Patagonia (Argentina). Oceanography 31, 92–103.

Dezileau, L., Bareille, G., Reyss, J.L., Lemoine, F., 2000. Evidence for strong sediment redistribution by bottom currents along the southeast Indian ridge. Deep Sea Research Part I: Oceanographic Research Papers 47, 1899–1936. https://doi.org/10.1016/S0967-0637(00)00008-X

995 Diekmann, B., 2007. Sedimentary patterns in the late Quaternary Southern Ocean. Deep Sea
996 Research Part II: Topical Studies in Oceanography 54, 2350–2366.
997 https://doi.org/10.1016/j.dsr2.2007.07.025

998 Diekmann, B., Kuhn, G., Rachold, V., Abelmann, A., Brathauer, U., Fütterer, D.K.,
999 Gersonde, R., Grobe, H., 2000. Terrigenous sediment supply in the Scotia Sea
1000 (Southern Ocean): response to Late Quaternary ice dynamics in Patagonia and on the
1001 Antarctic Peninsula. Palaeogeography, Palaeoclimatology, Palaeoecology 162, 357–
1002 387. https://doi.org/10.1016/S0031-0182(00)00138-3

1003 Engler, A., 2009. The Geology of South America, in: Geology. Encyclopedia of Life Support
1004 Systems, p. 11.

1005 Esquevin, J., 1969. Influence de la composition chimique des illites sur leur cristallinité. Bull.
1006 Centre Rech. Pau-SNPA 3, 147–153.

1007 Fischer, H., Schmitt, J., Lüthi, D., Stocker, T.F., Tschumi, T., Parekh, P., Joos, F., Köhler, P.,
1008 Völker, C., Gersonde, R., Barbante, C., Le Floch, M., Raynaud, D., Wolff, E., 2010.
1009 The role of Southern Ocean processes in orbital and millennial CO2 variations – A
1010 synthesis. Quaternary Science Reviews 29, 193–205.
1011 https://doi.org/10.1016/j.quascirev.2009.06.007

1012 Flowerdew, M.J., Tyrrell, S., Riley, T.R., Whitehouse, M.J., Mulvaney, R., Leat, P.T.,
1013 Marschall, H.R., 2012. Distinguishing East and West Antarctic sediment sources using
1014 the Pb isotope composition of detrital K-feldspar. Chemical Geology 292–293, 88–
1015 102. https://doi.org/10.1016/j.chemgeo.2011.11.006

1016 Foster, T.D., Carmack, E.C., 1976. Frontal zone mixing and Antarctic Bottom water
1017 formation in the southern Weddell Sea. Deep Sea Research and Oceanographic
1018 Abstracts 23, 301–317. https://doi.org/10.1016/0011-7471(76)90872-X

1019 Fretzdorff, S., Livermore, R.A., Devey, C.W., Leat, P.T., Stoffers, P., 2002. Petrogenesis of
1020 the back-arc east scotia ridge, south Atlantic ocean. Journal of Petrology 43, 1435–
1021 1467. https://doi.org/10.1093/petrology/43.8.1435

1022 Fuck, R.A., Dantas, E.L., Pimentel, M.M., Botelho, N.F., Armstrong, R., Laux, J.H., Junges,
1023 S.L., Soares, J.E., Praxedes, I.F., 2014. Paleoproterozoic crust-formation and
1024 reworking events in the Tocantins Province, central Brazil: A contribution for
1025 Atlantica supercontinent reconstruction. Precambrian Research 244, 53–74.
1026 https://doi.org/10.1016/j.precamres.2013.12.003

1027 Ganade de Araujo, C.E., Cordani, U.G., Weinberg, R.F., Basei, M.A.S., Armstrong, R., Sato,
1028 K., 2014. Tracing Neoproterozoic subduction in the Borborema Province (NE-Brazil):
1029 Clues from U-Pb geochronology and Sr-Nd-Hf-O isotopes on granitoids and
1030 migmatites. Lithos 202–203, 167–189. https://doi.org/10.1016/j.lithos.2014.05.015

1031 Gersonde, R., Abelmann, A., Brathauer, U., Becquey, S., Bianchi, C., Cortese, G., Grobe, H.,
1032 Kuhn, G., Niebler, H.-S., Segl, M., Sieger, R., Zielinski, U., Fütterer, D.K., 2003. Last
1033 glacial sea surface temperatures and sea-ice extent in the Southern Ocean (Atlantic-
1034 Indian sector): A multiproxy approach. Paleoceanography 18.
1035 https://doi.org/10.1029/2002PA000809

1036 Gherardi, J.-M., Labeyrie, L., Nave, S., Francois, R., McManus, J.F., Cortijo, E., 2009.
1037 Glacial-interglacial circulation changes inferred from 231Pa/230Th sedimentary
1038 record in the North Atlantic region. Paleoceanography 24.
1039 https://doi.org/10.1029/2008PA001696

1040 Gottschalk, J., Skinner, L.C., Lippold, J., Vogel, H., Frank, N., Jaccard, S.L., Waelbroeck, C.,
1041 2016. Biological and physical controls in the Southern Ocean on past millennial-scale

1042 atmospheric CO2 changes. Nature Communications 7, 11539.
1043 https://doi.org/10.1038/ncomms11539

1044 Gottschalk, J., Skinner, L.C., Misra, S., Waelbroeck, C., Menviel, L., Timmermann, A.,
1045 2015a. Abrupt changes in the southern extent of North Atlantic Deep Water during
1046 Dansgaard–Oeschger events. Nature Geoscience 8, 950.
1047 https://doi.org/10.1038/NGEO2558

1048 Gottschalk, J., Skinner, L.C., Waelbroeck, C., 2015b. Contribution of seasonal sub-Antarctic
1049 surface water variability to millennial-scale changes in atmospheric CO2 over the last
1050 deglaciation and Marine Isotope Stage 3. Earth and Planetary Science Letters 411, 87–
1051 99. https://doi.org/10.1016/j.epsl.2014.11.051

1052 Govin, A., Michel, E., Labeyrie, L., Waelbroeck, C., Dewilde, F., Jansen, E., 2009. Evidence
1053 for northward expansion of Antarctic Bottom Water mass in the Southern Ocean
1054 during the last glacial inception. Paleoceanography 24.
1055 https://doi.org/10.1029/2008PA001603

1056 Grousset, F.E., Rognon, P., Coudé-Gaussen, G., Pédemay, P., 1992. Origins of peri-Saharan
1057 dust deposits traced by their Nd and Sr isotopic composition. Palaeogeography,
1058 Palaeoclimatology, Palaeoecology 93, 203–212. https://doi.org/10.1016/0031-
1059 0182(92)90097-O

1060 Guyot, J.L., Jouanneau, J.M., Soares, L., Boaventura, G.R., Maillet, N., Lagane, C., 2007.
1061 Clay mineral composition of river sediments in the Amazon Basin. CATENA 71, 340–
1062 356. https://doi.org/10.1016/j.catena.2007.02.002

1063 Hall, I.R., McCave, I.N., Shackleton, N.J., Weedon, G.P., Harris, S.E., 2001. Intensified deep
1064 Pacific inflow and ventilation in Pleistocene glacial times. Nature 412, 809–812.
1065 https://doi.org/10.1038/35090552

Harrison, D., Leat, P.T., Burnard, P.G., Turner, G., Fretzdorff, S., Millar, I.L., 2003. Resolving mantle components in oceanic lavas from segment E2 of the East Scotia back-arc ridge, South Sandwich Islands. Geological Society, London, Special Publications 219, 333. https://doi.org/10.1144/GSL.SP.2003.219.01.16

Hauptvogel, D.W., Passchier, S., 2012. Early–Middle Miocene (17–14Ma) Antarctic ice dynamics reconstructed from the heavy mineral provenance in the AND-2A drill core, Ross Sea, Antarctica. Global and Planetary Change 82–83, 38–50. https://doi.org/10.1016/j.gloplacha.2011.11.003

Hegner, E., Dauelsberg, H.J., Rutgers Van Der Loeff, M.M., Jeandel, C., De Baar, H.J.W., 2007. Nd isotopic constraints on the origin of suspended particles in the Atlantic Sector of the Southern Ocean. Geochemistry, Geophysics, Geosystems 8. https://doi.org/10.1029/2007GC001666

Hole, M.J., Kempton, P.D., Millar, I.L., 1993. Trace-element and isotopic characteristics of small-degree melts of the asthenosphere: Evidence from the alkalic basalts of the Antarctic Peninsula. Chemical Geology 109, 51–68. https://doi.org/10.1016/0009-2541(93)90061-M

Howard, W.R., Prell, W.L., 1992. Late Quaternary Surface Circulation of the Southern Indian Ocean and its Relationship to Orbital Variations. Paleoceanography 7, 79–117. https://doi.org/10.1029/91PA02994

Howe, J.N.W., Piotrowski, A.M., Noble, T.L., Mulitza, S., Chiessi, C.M., Bayon, G., 2016. North Atlantic Deep Water Production during the Last Glacial Maximum. Nature Communications 7, 11765. https://doi.org/10.1038/ncomms11765

Jaccard, S.L., Hayes, C.T., Martínez-García, A., Hodell, D.A., Anderson, R.F., Sigman, D.M., Haug, G.H., 2013. Two Modes of Change in Southern Ocean Productivity Over the Past Million Years. Science 339, 1419. https://doi.org/10.1126/science.1227545

Jeandel, C., Arsouze, T., Lacan, F., Téchiné, P., Dutay, J.-C., 2007. Isotopic Nd compositions and concentrations of the lithogenic inputs into the ocean: A compilation, with an emphasis on the margins. Chemical Geology 239, 156–164. https://doi.org/10.1016/j.chemgeo.2006.11.013

Khondoker, R., Weiss, D., van de Flierdt, T., Rehkämper, M., Kreissig, K., Coles, B.J., Strekopytov, S., Humphreys-Williams, E., Dong, S., Bory, A., Bout-Roumazeilles, V., Smichowski, P., Cid-Agüero, P., Babinski, M., Losno, R., Monna, F., 2018. New constraints on elemental and Pb and Nd isotope compositions of South American and Southern African aerosol sources to the South Atlantic Ocean. Geochemistry 78, 372–384. https://doi.org/10.1016/j.chemer.2018.05.001

Köhler, P., Fischer, H., 2006. Simulating low frequency changes in atmospheric CO2 during the last 740 000 years. Climate of the Past 2, 57–78.

Košler, J., Magna, T., Mlčoch, B., Mixa, P., Nývlt, D., Holub, F.V., 2009. Combined Sr, Nd, Pb and Li isotope geochemistry of alkaline lavas from northern James Ross Island (Antarctic Peninsula) and implications for back-arc magma formation. Chemical Geology 258, 207–218. https://doi.org/10.1016/j.chemgeo.2008.10.006

Krueger, S., Leuschner, D.C., Ehrmann, W., Schmiedl, G., Mackensen, A., 2012. North Atlantic Deep Water and Antarctic Bottom Water variability during the last 200ka recorded in an abyssal sediment core off South Africa. Global and Planetary Change 80–81, 180–189. https://doi.org/10.1016/j.gloplacha.2011.10.001

1111 Krueger, S., Leuschner, D.C., Ehrmann, W., Schmiedl, G., Mackensen, A., Diekmann, B.,
1112 2008. Ocean circulation patterns and dust supply into the South Atlantic during the last
1113 glacial cycle revealed by statistical analysis of kaolinite/chlorite ratios. Marine
1114 Geology 253, 82–91. https://doi.org/10.1016/j.margeo.2008.04.015

1115 Kuhn, G., Diekmann, B., 2002. Late Quaternary variability of ocean circulation in the
1116 southeastern South Atlantic inferred from the terrigenous sediment record of a drift
1117 deposit in the southern Cape Basin (ODP Site 1089). Palaeogeography,
1118 Palaeoclimatology, Palaeoecology 182, 287–303. https://doi.org/10.1016/S0031-
1119 0182(01)00500-4

1120 Laird, M.G., 1991. The late Proterozoic-middle Palaeozoic rocks of Antarctica, in: The
1121 Geology of Antarctica. pp. 74–119.

1122 Lambert, F., Delmonte, B., Petit, J.R., Bigler, M., Kaufmann, P.R., Hutterli, M.A., Stocker,
1123 T.F., Ruth, U., Steffensen, J.P., Maggi, V., 2008. Dust-climate couplings over the past
1124 800,000 years from the EPICA Dome C ice core. Nature 452, 616.
1125 https://doi.org/10.1038/nature06763

1126 Larqué, L., Maamaatuaiahutapu, K., Garçon, V., 1997. On the intermediate and deep water
1127 flows in the South Atlantic Ocean. Journal of Geophysical Research: Oceans 102,
1128 12425–12440.

1129 Le Quéré, C., Rödenbeck, C., Buitenhuis, E.T., Conway, T.J., Langenfelds, R., Gomez, A.,
1130 Labuschagne, C., Ramonet, M., Nakazawa, T., Metzl, N., Gillett, N., Heimann, M.,
1131 2007. Saturation of the Southern Ocean CO2 Sink Due to Recent Climate Change.
1132 Science 316, 1735. https://doi.org/10.1126/science.1136188

1133 Lee, J.I., Park, B.-K., Jwa, Y.-J., Ho Il Yoon, Kyu Chul Yoo, Kim, Y., 2005. Geochemical
1134 characteristics and the provenance of sediments in the Bransfield Strait, West
1135 Antarctica. Marine Geology 219, 81–98. https://doi.org/10.1016/j.margeo.2005.06.002

1136 Luttinen, A.V., Leat, P.T., Furnes, H., 2010. Björnnutane and Sembberget basalt lavas and the
1137 geochemical provinciality of Karoo magmatism in western Dronning Maud Land,
1138 Antarctica. Journal of Volcanology and Geothermal Research 198, 1–18.
1139 https://doi.org/10.1016/j.jvolgeores.2010.07.011

1140 Luttinen, A.V., Rämö, O.T., Huhma, H., 1998. Neodymium and strontium isotopic and trace
1141 element composition of a Mesozoic CFB suite from Dronning Maud Land, Antarctica:
1142 implications for lithosphere and asthenosphere contributions to Karoo magmatism.
1143 Geochimica et Cosmochimica Acta 62, 2701–2714. https://doi.org/10.1016/S0016-
1144 7037(98)00184-7

1145 Mallmann, G., Chemale, F., Ávila, J.N., Kawashita, K., Armstrong, R.A., 2007. Isotope
1146 geochemistry and geochronology of the Nico Pérez Terrane, Rio de la Plata Craton,
1147 Uruguay. Gondwana Research 12, 489–508. https://doi.org/10.1016/j.gr.2007.01.002

1148 Martínez-García, A., Sigman, D.M., Ren, H., Anderson, R.F., Straub, M., Hodell, D.A.,
1149 Jaccard, S.L., Eglinton, T.I., Haug, G.H., 2014. Iron Fertilization of the Subantarctic
1150 Ocean During the Last Ice Age. Science 343, 1347.
1151 https://doi.org/10.1126/science.1246848

1152 Mathias, G.L., Nagai, R.H., Trindade, R.I.F., de Mahiques, M.M., 2014. Magnetic fingerprint
1153 of the late Holocene inception of the Río de la Plata plume onto the southeast
1154 Brazilian shelf. Palaeogeography, Palaeoclimatology, Palaeoecology 415, 183–196.
1155 https://doi.org/10.1016/j.palaeo.2014.03.034

1156 Mazaud, A., Michel, E., Dewilde, F., Turon, J.L., 2010. Variations of the Antarctic
1157 Circumpolar Current intensity during the past 500 ka. Geochemistry, Geophysics,
1158 Geosystems 11. https://doi.org/10.1029/2010GC003033

1159 McCave, I.N., Andrews, J.T., 2019. Distinguishing current effects in sediments delivered to
1160 the ocean by ice. I. Principles, methods and examples. Quaternary Science Reviews
1161 212, 92–107. https://doi.org/10.1016/j.quascirev.2019.03.031

1162 McCave, I.N., Crowhurst, S.J., Kuhn, G., Hillenbrand, C.-D., Meredith, M.P., 2014. Minimal
1163 change in Antarctic Circumpolar Current flow speed between the last glacial and
1164 Holocene. Nature Geoscience 7, 113. https://doi.org/10.1038/ngeo2037

1165 McCave, I.N., Hall, I.R., 2006. Size sorting in marine muds: Processes, pitfalls, and prospects
1166 for paleoflow-speed proxies: SIZE SORTING IN MARINE MUDS. Geochem.
1167 Geophys. Geosyst. 7, n/a-n/a. https://doi.org/10.1029/2006GC001284

1168 McGee, B., Collins, A.S., Trindade, R.I.F., Jourdan, F., 2015. Investigating mid-Ediacaran
1169 glaciation and final Gondwana amalgamation using coupled sedimentology and 40Ar/
1170 39Ar detrital muscovite provenance from the Paraguay Belt, Brazil. Sedimentology
1171 62, 130–154. https://doi.org/10.1111/sed.12143

1172 Menviel, L., England, M.H., Meissner, K.J., Mouchet, A., Yu, J., 2014. Atlantic-Pacific
1173 seesaw and its role in outgassing CO2 during Heinrich events. Paleoceanography 29,
1174 58–70. https://doi.org/10.1002/2013PA002542

1175 Menviel, L., Joos, F., Ritz, S.P., 2012. Modeling atmospheric CO2, stable carbon isotope and
1176 marine carbon cycle changes during the last glacial-interglacial cycle. Quat. Sci. Rev
1177 56, 46–68.

1178 Menviel, L., Spence, P., England, M.H., 2015. Contribution of enhanced Antarctic Bottom
1179 Water formation to Antarctic warm events and millennial-scale atmospheric CO2

1180 increase. Earth and Planetary Science Letters 413, 37–50.
1181 https://doi.org/10.1016/j.epsl.2014.12.050

1182 Menviel, Laurie, Spence, P., Golledge, N., England, M.H., 2015. Southern Ocean Overturning
1183 Role in Modulating High Southern Latitude Climate and Atmospheric CO2 on
1184 Millennial Timescales. Nova Acta Leopoldina NF 121, 159–166.

1185 Menviel, L., Spence, P., Yu, J., Chamberlain, M.A., Matear, R.J., Meissner, K.J., England,
1186 M.H., 2018. Southern Hemisphere westerlies as a driver of the early deglacial
1187 atmospheric CO2 rise. Nature Communications 9, 2503.
1188 https://doi.org/10.1038/s41467-018-04876-4

1189 Menviel, L., Yu, J., Joos, F., Mouchet, A., Meissner, K.J., England, M.H., 2017. Poorly
1190 ventilated deep ocean at the Last Glacial Maximum inferred from carbon isotopes: A
1191 data-model comparison study. Paleoceanography 32, 2–17.
1192 https://doi.org/10.1002/2016PA003024

1193 Meyer, I., Davies, G.R., Stuut, J.-B.W., 2011. Grain size control on Sr-Nd isotope provenance
1194 studies and impact on paleoclimate reconstructions: An example from deep-sea
1195 sediments offshore NW Africa. Geochemistry, Geophysics, Geosystems 12.
1196 https://doi.org/10.1029/2010GC003355

1197 Mieth, M., Jokat, W., 2014. Banded iron formation (?) at Grunehogna Craton, East Antarctica
1198 – Constraints from aeromagnetic data. Precambrian Research 250, 143–150.
1199 https://doi.org/10.1016/j.precamres.2014.06.001

1200 Milani, E.J., Ramos, V.A., 2017. Orogenias paleozóicas no domínio sul-ocidental do
1201 Gondwana e os ciclos de subsidência da Bacia do Paraná. Revista Brasileira de
1202 Geociências 28, 473–484.

1203 Missiaen, L., Waelbroeck, C., Pichat, S., Jaccard, S.L., Eynaud, F., Greenop, R., Burke, A.,
1204 2019. Improving North Atlantic marine core chronologies using 230Th-normalization.
1205 Paleoceanography and Paleoclimatology 0. https://doi.org/10.1029/2018PA003444

1206 Montero-Serrano, J.C., Bout-Roumazeilles, V., Sionneau, T., Tribovillard, N., Bory, A.,
1207 Flower, B.P., Riboulleau, A., Martinez, P., Billy, I., 2010. Changes in precipitation
1208 regimes over North America during the Holocene as recorded by mineralogy and
1209 geochemistry of Gulf of Mexico sediments. Global and Planetary Change 74, 132–
1210 143. https://doi.org/10.1016/j.gloplacha.2010.09.004

1211 Montero-Serrano, J.C., Bout-Roumazeilles, V., Tribovillard, N., Sionneau, T., Riboulleau, A.,
1212 Bory, A., Flower, B., 2009. Sedimentary evidence of deglacial megafloods in the
1213 northern Gulf of Mexico (Pigmy Basin). Quaternary Science Reviews 28, 3333–3347.
1214 https://doi.org/10.1016/j.quascirev.2009.09.011

1215 Moriarty, K.C., 1977. Clay minerals in Southeast Indian Ocean sediments, transport
1216 mechanisms and depositional environments. Marine Geology 25, 149–174.
1217 https://doi.org/10.1016/0025-3227(77)90051-2

1218 Moura, C.A., Gaudette, H., 1993. Evidence of Brasiliano/Panafrican deformation in the
1219 Araguaia belt: implication for Gondwana evolution. Rev. Bras. Geoc 23, 117–123.

1220 Neves, S.P., 2003. Proterozoic history of the Borborema province (NE Brazil): Correlations
1221 with neighboring cratons and Pan-African belts and implications for the evolution of
1222 western Gondwana. Tectonics 22. https://doi.org/10.1029/2001TC001352

1223 Noble, T.L., Piotrowski, A.M., Robinson, L.F., McManus, J.F., Hillenbrand, C.-D., Bory,
1224 A.J.-M., 2012. Greater supply of Patagonian-sourced detritus and transport by the
1225 ACC to the Atlantic sector of the Southern Ocean during the last glacial period. Earth

and Planetary Science Letters 317–318, 374–385. https://doi.org/10.1016/j.epsl.2011.10.007

Nogueira, A.C.R., Riccomini, C., Sial, A.N., Moura, C.A.V., Trindade, R.I.F., Fairchild, T.R., 2007. Carbon and strontium isotope fluctuations and paleoceanographic changes in the late Neoproterozoic Araras carbonate platform, southern Amazon craton, Brazil. Chemical Geology 237, 168–190. https://doi.org/10.1016/j.chemgeo.2006.06.016

Olivero, E.B., Martinioni, D.R., 2001. A review of the geology of the Argentinian Fuegian Andes. Journal of South American Earth Sciences, Mesozoic Palaeontology and Stratigraphy of South America and the South Atlantic 14, 175–188. https://doi.org/10.1016/S0895-9811(01)00016-5

Orsi, A.H., Johnson, G.C., Bullister, J.L., 1999. Circulation, mixing, and production of Antarctic Bottom Water. Progress in Oceanography 43, 55–109. https://doi.org/10.1016/S0079-6611(99)00004-X

Oyhantçabal, P., Siegesmund, S., Wemmer, K., 2011. The Río de la Plata Craton: a review of units, boundaries, ages and isotopic signature. International Journal of Earth Sciences 100, 201–220. https://doi.org/10.1007/s00531-010-0580-8

Petschick, R., 2000. MacDiff 4.2. 5.

Petschick, R., Kuhn, G., Gingele, F., 1996. Clay mineral distribution in surface sediments of the South Atlantic: sources, transport, and relation to oceanography. Marine Geology 130, 203–229. https://doi.org/10.1016/0025-3227(95)00148-4

Pierce, E.L., Hemming, S.R., Williams, T., van de Flierdt, T., Thomson, S.N., Reiners, P.W., Gehrels, G.E., Brachfeld, S.A., Goldstein, S.L., 2014. A comparison of detrital U–Pb zircon, 40Ar/39Ar hornblende, 40Ar/39Ar biotite ages in marine sediments off East

1249 Antarctica: Implications for the geology of subglacial terrains and provenance studies.
1250 Earth-Science Reviews 138, 156–178. https://doi.org/10.1016/j.earscirev.2014.08.010

1251 Pimentel, M.M., Rodrigues, J.B., DellaGiustina, M.E.S., Junges, S., Matteini, M., Armstrong,
1252 R., 2011. The tectonic evolution of the Neoproterozoic Brasília Belt, central Brazil,
1253 based on SHRIMP and LA-ICPMS U–Pb sedimentary provenance data: A review.
1254 Journal of South American Earth Sciences 31, 345–357.
1255 https://doi.org/10.1016/j.jsames.2011.02.011

1256 Reid, J.L., 1989. On the total geostrophic circulation of the South Atlantic Ocean: Flow
1257 patterns, tracers, and transports. Progress in Oceanography 23, 149–244.
1258 https://doi.org/10.1016/0079-6611(89)90001-3

1259 Roberts, J., Gottschalk, J., Skinner, L.C., Peck, V.L., Kender, S., Elderfield, H., Waelbroeck,
1260 C., Vázquez Riveiros, N., Hodell, D.A., 2016. Evolution of South Atlantic density and
1261 chemical stratification across the last deglaciation. Proc Natl Acad Sci USA 113, 514.
1262 https://doi.org/10.1073/pnas.1511252113

1263 Roy, M., van de Flierdt, T., Hemming, S.R., Goldstein, S.L., 2007. 40Ar/39Ar ages of
1264 hornblende grains and bulk Sm/Nd isotopes of circum-Antarctic glacio-marine
1265 sediments: Implications for sediment provenance in the southern ocean. Chemical
1266 Geology 244, 507–519. https://doi.org/10.1016/j.chemgeo.2007.07.017

1267 Sallée, J.B., Matear, R., Rintoul, S.R., Lenton, A., 2012. Surface to interior pathways of
1268 anthropogenic CO2 in the southern hemisphere oceans. Nat. Geosci. 5, 579–584.

1269 Sayago, J.M., Collantes, M.M., Karlson, A., Sanabria, J., 2001. Genesis and distribution of
1270 the Late Pleistocene and Holocene loess of Argentina: a regional approximation.
1271 Quaternary International 76–77, 247–257. https://doi.org/10.1016/S1040-
1272 6182(00)00107-5

1273 Shakun, J.D., Clark, P.U., He, F., Marcott, S.A., Mix, A.C., Liu, Z., Otto-Bliesner, B.,
1274 Schmittner, A., Bard, E., 2012. Global warming preceded by increasing carbon
1275 dioxide concentrations during the last deglaciation. Nature 484, 49.
1276 https://doi.org/10.1038/nature10915

1277 Siani, G., Michel, E., De Pol-Holz, R., DeVries, T., Lamy, F., Carel, M., Isguder, G.,
1278 Dewilde, F., Lourantou, A., 2013. Carbon isotope records reveal precise timing of
1279 enhanced Southern Ocean upwelling during the last deglaciation. Nature
1280 Communications 4, 2758.

1281 Siegesmund, S., Basei, M., Oyhantçabal, P., 2011. Multi-accretional tectonics at the Rio de la
1282 Plata Craton margins: preface. International Journal of Earth Sciences 100, 197–200.
1283 https://doi.org/10.1007/s00531-010-0616-0

1284 Skinner, L.C., Fallon, S., Waelbroeck, C., Michel, E., Barker, S., 2010. Ventilation of the
1285 Deep Southern Ocean and Deglacial CO2 Rise. Science 328, 1147.
1286 https://doi.org/10.1126/science.1183627

1287 Skinner, L.C., Scrivner, A.E., Vance, D., Barker, S., Fallon, S., Waelbroeck, C., 2013. North
1288 Atlantic versus Southern Ocean contributions to a deglacial surge in deep ocean
1289 ventilation. Geology 41, 667–670. https://doi.org/10.1130/G34133.1

1290 Skinner, L.C., Waelbroeck, C., Scrivner, A.E., Fallon, S.J., 2014. Radiocarbon evidence for
1291 alternating northern and southern sources of ventilation of the deep Atlantic carbon
1292 pool during the last deglaciation. Proc Natl Acad Sci USA 111, 5480.
1293 https://doi.org/10.1073/pnas.1400668111

1294 Smith, J., Vance, D., Kemp, R.A., Archer, C., Toms, P., King, M., Zárate, M., 2003. Isotopic
1295 constraints on the source of Argentinian loess – with implications for atmospheric
1296 circulation and the provenance of Antarctic dust during recent glacial maxima. Earth

and Planetary Science Letters 212, 181–196. https://doi.org/10.1016/S0012-821X(03)00260-7

Speer, K.G., Zenk, W., 1993. The Flow of Antarctic Bottom Water into the Brazil Basin. J. Phys. Oceanogr. 23, 2667–2682. https://doi.org/10.1175/1520-0485(1993)023<2667:TFOABW>2.0.CO;2

Spooner, P.T., Thornalley, D.J.R., Ellis, P., 2018. Grain Size Constraints on Glacial Circulation in the Southwest Atlantic. Paleoceanography and Paleoclimatology 33, 21–30. https://doi.org/10.1002/2017PA003232

Stern, C.R., Frey, F.A., Futa, K., Zartman, R.E., Peng, Z., Kurtis Kyser, T., 1990. Trace-element and Sr, Nd, Pb, and O isotopic composition of Pliocene and Quaternary alkali basalts of the Patagonian Plateau lavas of southernmost South America. Contributions to Mineralogy and Petrology 104, 294–308. https://doi.org/10.1007/BF00321486

Stramma, L., England, M., 1999. On the water masses and mean circulation of the South Atlantic Ocean. Journal of Geophysical Research: Oceans 104, 20863–20883. https://doi.org/10.1029/1999JC900139

Tapani Rämö, O., Heikkilä, P.A., Pulkkinen, A.H., 2016. Geochemistry of Paraná-Etendeka basalts from Misiones, Argentina: Some new insights into the petrogenesis of high-Ti continental flood basalts. Journal of South American Earth Sciences 67, 25–39. https://doi.org/10.1016/j.jsames.2016.01.008

Tingey, R.J., 1991. The regional geology of Archean and Proterozoic rocks in Antractica., in: The Geology of Antarctica. Oxford University Press, pp. 1–73.

Tingey, R.J., Laird, M.J., Barret, P.J., Ford, A.B., Himmelberg, P.F., Barker, P.F., Dalziel, I.W., Storey, B.C., LeMasurier, W.E., Rex, D.C., Anderson, J.B., Bentley, C.R., Denton, G.H., Prentice, M.L., Burckle, L.H., McKelvey, B.C., Cooper, R.A.,

Shergold, J.H., Thomson, M.R.A., Truswell, E.M., Young, G.C., Colbert, E.H., Behrent, J.C., Rowler, P.D., Williams, P.L., Pride, D.E., Cassidy, W.A., 1991. The geology of Antarctica. Oxford University Press.

Toggweiler, J.R., Russell, J.L., Carson, S.R., 2006. Midlatitude westerlies, atmospheric CO2, and climate change during the ice ages. Paleoceanography 21. https://doi.org/10.1029/2005PA001154

van de Flierdt, T., Goldstein, S.L., Hemming, S.R., Roy, M., Frank, M., Halliday, A.N., 2007. Global neodymium–hafnium isotope systematics — revisited. Earth and Planetary Science Letters 259, 432–441. https://doi.org/10.1016/j.epsl.2007.05.003

Vázquez Riveiros, N., Waelbroeck, C., Skinner, L., Roche, D.M., Duplessy, J.-C., Michel, E., 2010. Response of South Atlantic deep waters to deglacial warming during Terminations V and I. Earth and Planetary Science Letters 298, 323–333. https://doi.org/10.1016/j.epsl.2010.08.003

Waelbroeck, C., Skinner, L.C., Labeyrie, L., Duplessy, J.-C., Michel, E., Vazquez Riveiros, N., Gherardi, J.-M., Dewilde, F., 2011. The timing of deglacial circulation changes in the Atlantic. Paleoceanography 26. https://doi.org/10.1029/2010PA002007

Waichel, B.L., de Lima, E.F., Viana, A.R., Scherer, C.M., Bueno, G.V., Dutra, G., 2012. Stratigraphy and volcanic facies architecture of the Torres Syncline, Southern Brazil, and its role in understanding the Paraná–Etendeka Continental Flood Basalt Province. Journal of Volcanology and Geothermal Research 215–216, 74–82. https://doi.org/10.1016/j.jvolgeores.2011.12.004

Walter, H.J., Hegner, E., Diekmann, B., Kuhn, G., Rutgers van der loeff, M.M., 2000. Provenance and transport of terrigenous sediment in the south Atlantic Ocean and their

relations to glacial and interglacial cycles: Nd and Sr isotopic evidence. Geochimica et Cosmochimica Acta 64, 3813–3827. https://doi.org/10.1016/S0016-7037(00)00476-2

Watson, A.J., Bakker, D.C.E., Ridgwell, A.J., Boyd, P.W., Law, C.S., 2000. Effect of iron supply on Southern Ocean CO2 uptake and implications for glacial atmospheric CO2. Nature 407, 730–733. https://doi.org/10.1038/35037561

Weber, S.L., Drijfhout, S.S., 2007. Stability of the Atlantic Meridional Overturning Circulation in the Last Glacial Maximum climate. Geophysical Research Letters 34. https://doi.org/10.1029/2007GL031437

Weltje, G.J., 2012. Quantitative models of sediment generation and provenance: State of the art and future developments. Sedimentary Geology 280, 4–20. https://doi.org/10.1016/j.sedgeo.2012.03.010

Weltje, G.J., Prins, M.A., 2007. Genetically meaningful decomposition of grain-size distributions. Sedimentary Geology 202, 409–424. https://doi.org/10.1016/j.sedgeo.2007.03.007

Will, T.M., Frimmel, H.E., Zeh, A., Le Roux, P., Schmädicke, E., 2010. Geochemical and isotopic constraints on the tectonic and crustal evolution of the Shackleton Range, East Antarctica, and correlation with other Gondwana crustal segments. Precambrian Research 180, 85–112. https://doi.org/10.1016/j.precamres.2010.03.005

Wolff, E.W., Fischer, H., Fundel, F., Ruth, U., Twarloh, B., Littot, G.C., Mulvaney, R., Röthlisberger, R., de Angelis, M., Boutron, C.F., Hansson, M., Jonsell, U., Hutterli, M.A., Lambert, F., Kaufmann, P., Stauffer, B., Stocker, T.F., Steffensen, J.P., Bigler, M., Siggaard-Andersen, M.L., Udisti, R., Becagli, S., Castellano, E., Severi, M., Wagenbach, D., Barbante, C., Gabrielli, P., Gaspari, V., 2006. Southern Ocean sea-ice

extent, productivity and iron flux over the past eight glacial cycles. Nature 440, 491–496. https://doi.org/10.1038/nature04614

Supplementary figures

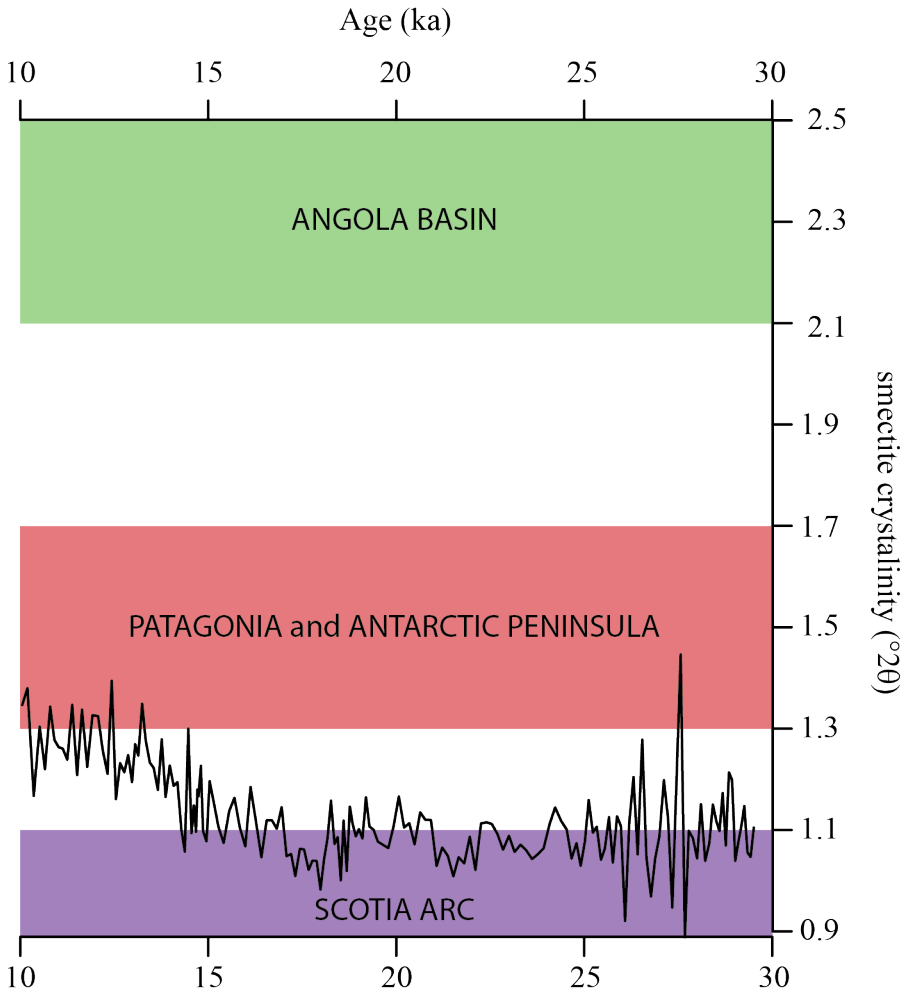

SUPPLEMENTARY FIGURE S1: Crystallinity of smectite from site MD07-3076Q (black curve) and comparison with crystallinity of smectite from potential sources to the South Atlantic basin. The data used for comparison are from Petschick et al., 1996.

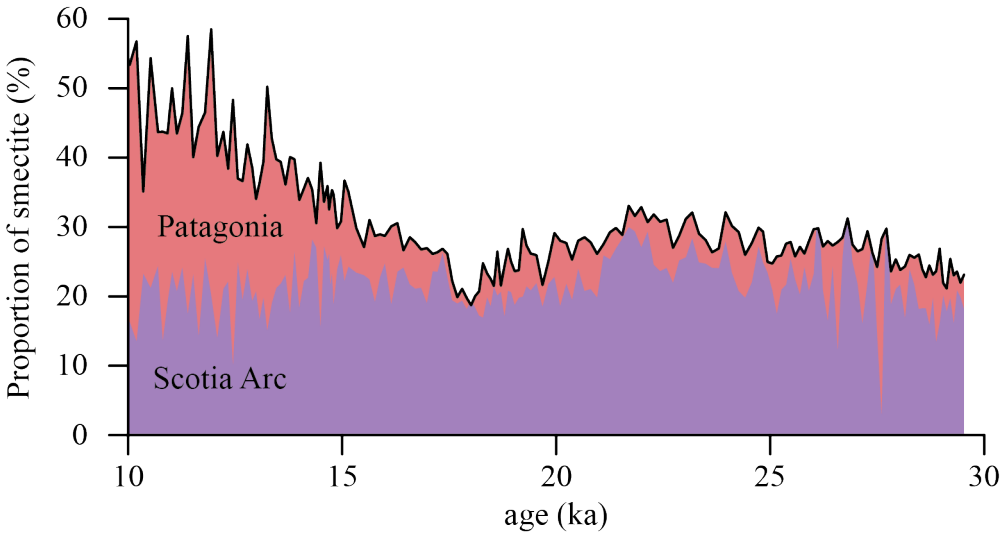

SUPPLEMENTARY FIGURE S2: Contribution of the two types of smectite from site MD07-3076Q. The black line represent the total smectite content, the purple area represent the smectite content from the Scotia Arc, and the red area represent the smectite content from Patagonia. The proportion of the two types of smectite are calculated as followed:

$$[\%\text{Patagonian smectite}] = [\%\text{total smectite}] \times \frac{(\text{sample crystallinity}] - (\text{Scotia Sea crystallinity}]}{(\text{Patagonia crystallinity}] - (\text{Scotia Sea crystallinity}]} \times 100$$

$$[\%\text{Scotia Sea smectite}] = [\%\text{total smectite}] - (\%\text{Patagonian smectite}]$$

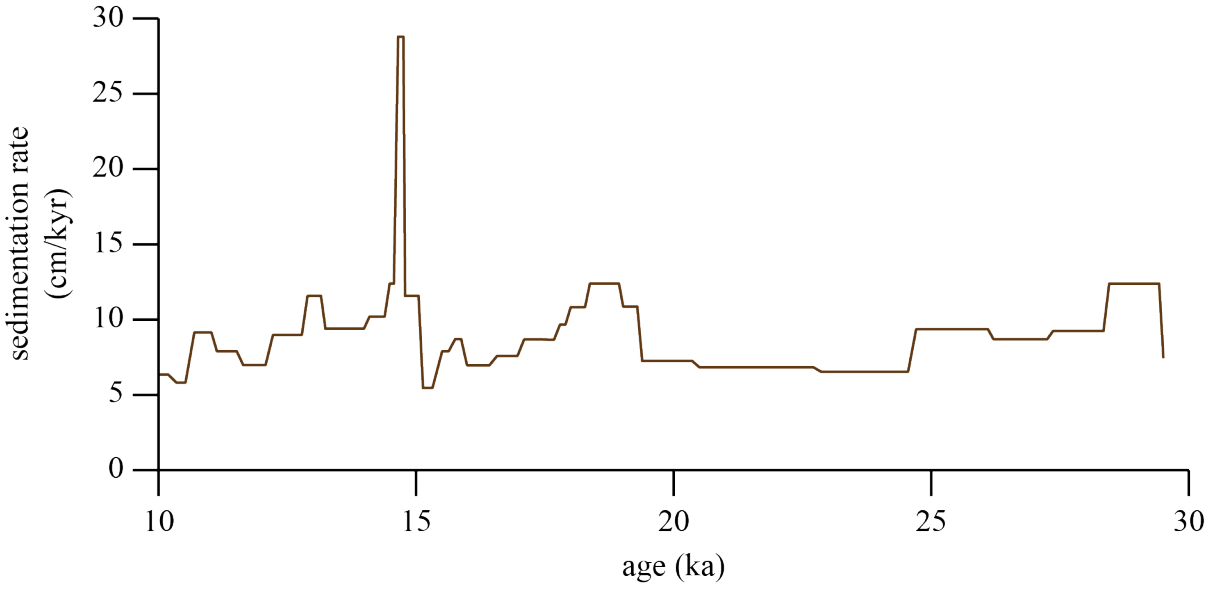

SUPPLEMENTARY FIGURE S3: Sedimentation rate from site MD07-3076Q calculated from the age model published in Skinner et al. (2010, 2013, 2014) and Gottschalk et al. (2015b).

Tables

	average (10-30 ka)	LGM (25-17 ka)	Deglaciation (17-11.7 ka)	standard deviation (10-30 ka)
fine mode (μm)	6.8	7.2	6.3	0.8
coarse mode (μm)	30.4	31.3	30.4	2.5
clay fraction (%)	3.4	3.0	3.8	0.7
sortable silts (10-63 μm; %)	47.0	47.2	46.2	2.4
cohesive silts (2-10 μm; %)	39.4	38.8	40.2	2.4
sand (%)	3.0	3.5	2.6	1.0
smectite (%)	30.7	26.7	35.7	7.9
illite (%)	33.5	34.7	31.7	3.3
chlorite (%)	25.1	27.2	22.3	4.2
kaolinite (%)	10.6	11.4	10.3	1.3
I/S	1.2	1.3	0.9	0.3
K/C	0.4	0.4	0.5	0.1
ε_{Nd} (<2 μm)	-5.8	-5.0	-6.0	0.8
ε_{Nd} (fine mode)	-4.6	-4.6	-4.7	0.4
ε_{Nd} (coase mode)	-3.3	-1.8	-3.7	1.2
$^{87}Sr/^{86}Sr$ (<2 μm)	0.71130	0.71144	0.71136	0.00036
$^{87}Sr/^{86}Sr$ (fine mode)	0.70795	0.70800	0.70798	0.00019
$^{87}Sr/^{86}Sr$ (coase mode)	0.70889	0.70859	0.70926	0.00058
$^{208}Pb/^{204}Pb$ (<2 μm)	38.774	38.775	38.785	0.012
$^{207}Pb/^{204}Pb$ (<2 μm)	15.644	15.639	15.645	0.008
$^{206}Pb/^{204}Pb$ (<2 μm)	18.752	18.749	18.758	0.030

TABLE 1: Average values of the different proxies for the entire record, the LGM, and the deglaciation.